Whole animal imaging

Gurpreet Singh Sandhu, **Luis Solorio**, **Ann-Marie Broome**, **Nicolas Salem**, **Jeff Kolthammer**, **Tejas Shah**, **Chris Flask**, and **Jeffrey L. Duerk**[*]

Department of Biomedical Engineering, Case Center of Imaging Research, Case Western Reserve University, Cleveland, OH 44106, USA

Abstract

Translational research plays a vital role in understanding the underlying pathophysiology of human diseases, and hence development of new diagnostic and therapeutic options for their management. After creating an animal disease model, pathophysiologic changes and effects of a therapeutic intervention on them are often evaluated on the animals using immunohistologic or imaging techniques. In contrast to the immunohistologic techniques, the imaging techniques are noninvasive and hence can be used to investigate the whole animal, oftentimes in a single exam which provides opportunities to perform longitudinal studies and dynamic imaging of the same subject, and hence minimizes the experimental variability, requirement for the number of animals, and the time to perform a given experiment. Whole animal imaging can be performed by a number of techniques including x-ray computed tomography, magnetic resonance imaging, ultrasound imaging, positron emission tomography, single photon emission computed tomography, fluorescence imaging, and bioluminescence imaging, among others. Individual imaging techniques provide different kinds of information regarding the structure, metabolism, and physiology of the animal. Each technique has its own strengths and weaknesses, and none serves every purpose of image acquisition from all regions of an animal. In this review, a broad overview of basic principles, available contrast mechanisms, applications, challenges, and future prospects of many imaging techniques employed for whole animal imaging is provided. Our main goal is to briefly describe the current state of art to researchers and advanced students with a strong background in the field of animal research.

In translational research, the gap between *in vitro* experiments and their clinical applications is often bridged by investigating the animal models of various human diseases. The pathophysiology of an animal and its response to a therapeutic intervention are often studied using one imaging technique or other. Most imaging techniques can be employed to perform transverse as well as longitudinal analyses of whole animals and this minimize the experimental variability, shorten the time required for a given experiment, and enable meaningful expenditure of research resources. Whole animal imaging can be performed using a number of imaging techniques. Depending upon their primary applications, the techniques for whole animal imaging can be broadly classified into two categories: structural and molecular imaging techniques. Structural imaging techniques primarily

[*]Correspondence to: jeffrey.duerk@case.edu.

provide high-resolution images in millimeter to micrometer range and include ultrasound (US) imaging, X-ray computed tomography (CT), and magnetic resonance imaging (MRI). Image formation in these techniques is based upon the principle of spatial difference in interactions of the tissues with sound waves, X-rays, and radiofrequency (RF) electromagnetic fields, respectively. The techniques of the second category are primarily employed for molecular imaging and can again be classified into two subcategories on the basis of the principle of image formation; in many ways, however, MRI and US share properties of both structural and molecular imaging. The first subcategory comprises of nuclear imaging techniques such as positron emission tomography (PET) and single photon emission computed tomography (SPECT), where the fundamental basis for image formation is detection of radiation emitted by injected radioactive tracers. The second subcategory consists of optical imaging techniques such as bioluminescence imaging (BLI), fluorescence imaging (FLI), and optical coherent tomography (OCT). The fundamental basis for image formation in BLI and FLI is capturing of a light photon emitted by a living microorganism or a fluorophore, respectively, from inside the animal. OCT exploits the difference in optical scattering properties of individual tissues for image formation. Individual imaging techniques provide different kinds of information regarding structure, metabolism, and physiology of an animal. Information provided by the individual techniques can be synergized by combining the images provided by them using an image registration mechanism.[1,2]

In this advanced review, an overview of the basic principle of image formation, contrast enhancement mechanisms, important applications, challenges, and future prospects of the techniques commonly employed for whole animal imaging is provided. Our main goal is to provide a brief description of the current state of art to the molecular biologists, biochemists, pathologists, geneticists, pharmacologists, and nuclear scientists who are working in the field of animal research. Information provided in this article would help these professionals in designing future experiments by considering the availability of these varied yet synergistic imaging techniques.

COMPUTED TOMOGRAPHY

Dedicated CT scanners employed for small animal imaging are a miniaturized version of clinical (human) CT scanners and are often called microcomputed tomogram (μCT) scanners.[3] For μCT image acquisition, a number of X-ray beams of a known intensity are projected onto an imaging volume of interest from different rotation angles. The intensity of the X-rays passing through the volume is captured by an array of X-ray detectors placed around it. Multiple X-ray projections acquired at different rotation angles are combined to produce the final μCT image. The image contrast between different tissues in the volume is determined by the difference in their individual X-rays attenuation capacity.[4] Knowledge of the intensity of the incident X-ray beam and that reaching the detectors allows the x-ray attenuating capacity of the tissue to be determined. Cardiorespiratory motion of the live animals during μCT image acquisition can be compensated by using prospective or retrospective respiratory and/or cardiac synchronization (i.e., gating).[5,6] A similar technique is digital subtraction angiography (DSA), in which an extracellular contrast agent is injected intravenously and data are acquired before and after contrast administration to generate

angiographic images. A projection image is obtained to display the distribution of the contrast agent by subtracting the precontrast image (i.e., a mask) from the post-contrast image.[4] Tomographic DSA has also been described in the literature to obtain 3D spatial information from DSA projections using tomosynthesis.[7]

Contrast Agents

The μCT contrast agents increase the degree of X-ray attenuation in the region of their distribution, and hence improve the μCT image contrast. Bolus injection of a clinically used iodine-based contrast agent such as Isovue-370 has been employed for small animal μCT imaging. Oftentimes, the volume of agent injected, the heart rate, blood flow, short circulation time, and the physiologic efficiency of renal excretion limit the amount of time the agents reside in small animal tissue. Therefore, it is sometimes difficult to obtain a sufficient number of projections for μCT imaging following a bolus injection of these agents.[8] Constant infusion of these contrast agents have been employed as an alternative to the bolus injection.[6]

New contrast agents with a relatively long vascular half-life are now available. Two iodinated triglycerides (glyceryl-2-oleoyl-1, 3-di-7-(3-amino- 2,4,6-triiodophenyl)-heptanoate; also called ITG-DHOG), Fenestra-VC and Fenestra-LC (iodine content 50 mg/ml) are currently employed as hepatobiliary-selective blood-pool contrast agents.[9,10] Fenestra-VC is particularly useful for cardiac, tumor, and hepatobiliary imaging.[5,11,12] Because of its rapid uptake by hepatocytes, Fenestra-LC has a very short blood-pool contrast enhancement time; however, it has found applications for spleen and hepatobiliary imaging.[13] Iodine-containing contrast agents are limited by the fact that they cannot be conjugated with biologic markers, which limits their utility for localization of specific targets.[8] This limitation of the iodine-containing contrast agents can be overcome by using nanoparticle-based contrast agents which can also be conjugated with biomarkers. Various nanoparticle-based contrast agents with a relatively long half-life such as polymer-coated gold nanoparticles,[14] gadolinium-coated gold nanoparticles,[15] Polyethylene glycol (PEG)-coated colloidal gold nanoparticles,[16] polymer-coated Bismuth-sulphide nanoparticles,[17] and antibody specific nanoprobes[8] have been developed for vascular imaging. Liposomal contrast agents have a long half-life[18] and a high affinity to microvascular fenestrations.[19] E-selectin-labeled liposomal contrast agents can be used to image activated endothelial cells.[20] Compounds such as tantalum[21] and xenon[22] have been employed as inhalation contrast agents.

Applications

μCT scanners can provide images at an almost cellular level of resolution[3] and have been employed for cardiac, pulmonary, hepatic, splenic, renal, and tumor imaging and to study gene expression. Cardiac μCT images can be obtained with a temporal and spatial resolution of up to 100 μm and 10 ms, respectively, using prospective gating[5] and up to 150 μm and 12 ms, respectively, using retrospective gating.[6] Recently, a registration-based approach for 4D (three spatial dimensions and one temporal) cardiac μCT imaging using a combined prospective and retrospective gating approach has also been introduced.[23] Various cardiac parameters can be calculated from dynamic μCT images by analyzing the left ventricular

volumes at different time points of the cardiac cycle.[5] Dynamic μCT cardiac imaging may be useful for understanding various pathologic processes such as left ventricular wall thickening [5] and temporal evaluation of myocardial infarction-induced cardiac remodeling.[24] μCT imaging has also been employed to investigate cardiac phenotype and coronary artery patterning defects.[25,26]

Small animal pulmonary μCT images with a spatial resolution as high as 91 μm and 150 μm have been obtained using prospective [27] and retrospective [22] gating, respectively. μCT images acquired at different time points in the respiratory cycle can be used to calculate the respiratory lung volumes [22] and morphometric indices.[17,22,28,29] μCT imaging has been employed to characterize pulmonary airways, pulmonary vasculature,[30] microvascular permeability, and alveolar membrane edema,[31] and for lung tumor analysis.[32,33] Small animal models of diseases such as emphysema [34] and fibrosis [24] have been investigated using μCT imaging.

μCT imaging of the liver and spleen is usually performed following contrast agent administration.[12,13,35] *In vivo* contrast-enhanced (CE) μCT images of liver with a spatial resolution as high as 44 μm have been produced and can be used to delineate tumors as small as 300 μm.[36,37] μCT imaging can also be used to delineate the hepatic vasculature [38] and investigate the changes following ischemic/reperfusion injury.[12] Iodinated liposomes are particularly useful for splenic μCT imaging because of the fact that they get degraded in the spleen. Red pulp of the spleen appears more radio-intense than white pulp in CE-μCT images as a result of concentration of phagocytes in the former.[35]

Renal μCT imaging is usually performed by *in situ* perfusion fixing and is particularly useful for glomerular analysis.[39–41] Conventional-source μCT scanners provide renal images with a spatial resolution in the range of 10–20 μm that can be used to calculate the total renal, cortical, and medullary volumes, glomerular diameters and numbers, and vascular volume fractions.[42,43] μCT images can also be used to visualize the 3D architecture of nephrons and renal blood vessels.[42,43]

In vivo μCT imaging of murine proximal tibial metaphysis has been performed with a spatial resolution as high as $20 \times 20 \times 26$ μm^3.[44] However, most of the previous work for osteology applications of μCT imaging has been done via *ex vivo* analysis. In addition to bone mineral content and bone mineral density, μCT images can be employed to calculate morphometric indices.[44–47] Longitudinal bone survey can also be performed in order to investigate the bone growth and unloading-related changes.[44,48]

μCT imaging is an important tool for longitudinal imaging of tumors (see Figure 1). μCT imaging has been used for hepatic [49] and pulmonary [50] tumor imaging. Gold nanoparticles conjugated with UM-A9 antibodies [8] and iodinated contrast agents such as Fenestra-VC [11] have also been employed for CE-μCT tumor imaging. E-selectin specific μCT imaging can be used to image activated vessel walls [20] and can be used for noninvasive monitoring of tumor angiogenesis.[51] Multiple-contrast[52] and negative-contrast[53] μCT colonography has also been devised to trace morphologic lesions and tumors in the murine colon *in vivo.* μCT imaging has also been employed to image the expression of sodium-iodide symporter (a

reporter gene) in mouse tumors.[54] Perfusion DSA has been employed to investigate vasculature flow patterns.[55,56] Pulmonary blood volume, blood flow, and mean transit times can be calculated from DSA images[4,7,56] (see Figure 2). DSA has also been employed to study tumor angiogenesis.[57] Tomographic DSA enables functional perfusion measurements in 4D.[7]

Challenges and Future Prospects

In order to understand human disease processes on the small animal models, acquired images need to be scaled according to dimensions and physiology of the animal;[4] hence, smaller volume elements (i.e., voxels) are required. Yet, the signal-to-noise ratio in the images is dependent on the number of X-ray photons passing through the voxel. As such, the X-ray exposure dose in μCT imaging of small animals can be high when compared to that in human imaging. In fact, as one might predict, higher X-ray exposure dose is detrimental to life expectancy of live animals, may alter phenotypic expression of genetically engineered animals, and can cause radiation-induced neoplasia.[3] Various approaches such as application of contrast agents, prospective gating, reduced X-ray scatter, monochromatic X-ray beams, fewer projections, alternate filtering, and beam modulation according to imaging cross section can be employed to decrease X-ray exposure dose.[5,58,59] Lastly, there are some daily practice challenges such as instrument availability, longer image acquisition times, and lower contrast agent availability that limit μCT utility.

The ability of μCT imaging to visualize the 3D architecture of basic functional units such as hepatic lobules and nephrons *in vivo* without physical disruption could help in further understanding the pathophysiology of various disease processes. Development of nanoparticles-based target-specific contrast agents would help in diagnosis of neoplastic lesions at the earlier stages. Newly developing refraction imaging techniques such as phase contrast imaging [60,61] can enable high-quality image acquisition with a potential reduction in the radiation exposure by as much as 10,000 fold.[58]

MAGNETIC RESONANCE IMAGING

Whole animal MRI can be performed on dedicated high-field MRI [62] and nuclear magnetic resonance (NMR) scanners as well as on clinical MRI scanners [63] using dedicated receiving coils.[64] During MRI acquisition, nuclei with a nonzero magnetic moment produce a net magnetization when placed within a static magnetic field (B_0) and are then excited by applying an RF excitation pulse. Following the excitation, the nuclei reemit RF waves that are spatially localized by applying magnetic field gradients of known magnitude and orientation.[65] A variety of morphologic images with different contrasts can be acquired by selecting a suitable combination of imaging sequence parameters.[66,67] In addition, various techniques such as contrast-enhanced (CE) MRI, perfusion MRI, functional MRI (fMRI), diffusion tensor imaging (DTI), and MR spectroscopy (MRS) can also be used to extract different kinds of information. CE-MRI involves image acquisition following injection of a gadolinium-based contrast agent. Two important CE-MRI techniques, dynamic contrast-enhanced (DCE) MRI [68] and dynamic susceptibility-contrast (DSC)-MRI[69] can be used to quantify contrast agent concentration by combining $T1$ (e.g., gadolinium chelates) and $T2*$ (e.g., iron oxide particles) agents with MR imaging acquisitions sensitive to the effects of

these specific agents. Perfusion MRI can be performed by any of the two methods, arterial spin labeling perfusion MRI (ASL-MRI) and DSC-MRI, and is used for perfusion quantification (regional blood flow and volume, etc.)[70] In ASL-MRI, the magnetization of a proton pool is labeled by applying a slice-selective RF pulse, and reduction of the signal in a $T1$–weighted image upon arrival of the magnetically labeled blood into the imaging volume is used for perfusion quantification.[71,72] A comparative analysis of ASL- and DSC-MRI techniques for perfusion MRI can be found elsewhere.[71] In fMRI, the activity-related neuronal activity changes in specific brain regions are indirectly and noninvasively analyzed. The concentration of oxyhemoglobin increases in the vicinity of neuronal excitation resulting in a signal increase in blood-oxygen-level-dependent MRI images.[73] In DTI, the magnitude and direction of water diffusivity is analyzed by comparing multiple images acquired with gradient pulses applied in different directions.[74] In this way, it is possible to map fiber direction information (e.g., brain white matter tracks). The fundamental basis for MRS is the shift in resonance frequencies of various paramagnetic atoms such as ^1H, ^{31}P, ^{13}C, ^{19}F, ^{17}O, and ^{23}Na as a result of the electronic environment of a given nuclei; for example, electronegative nuclei such as oxygen deshield detectable hydrogen nuclei of their respective electrons providing a different chemical shift from other electron-rich hydrogen nuclei (e.g., fat). With these and many othermolecular level differences, MRS provides the platform to explore the biochemistry of these atoms *in vivo*.[75–77]

Contrast Agents

Conventional MRI contrast agents influence the image contrast by reducing both the longitudinal ($T1$) as well as the transverse ($T2$) relaxation times of the water protons in their vicinity.[78] In this way, the contrast agents provide a positive and a negative contrast to the $T1$- and $T2$-weighted images, respectively. Detailed information regarding the mechanism of action, magnetic and chemical properties, and biodistribution pattern of various MRI contrast agents can be found elsewhere.[78] According to their magnetic properties, the MRI contrast agents can be classified as paramagnetic (e.g., gadolinium-based agents) or super-paramagnetic (e.g., iron oxide nanoparticles) agents.[78,79] Depending upon their biodistribution pattern, different contrast agents can be employed to image specific regions of the animal body. For example, conventional, FDA-approved, MRI contrast agents, such as gadolinium chelates, are extracellular agents that quickly distribute into the blood pool and interstitium following their intravenous injection. These agents do not cross the intact blood–brain barrier, and have found applications for imaging of MR angiography and enhancement of lesions such as tumors.[78] Blood-pool agents have a relatively large size and longer half-life in the blood than extracellular fluid (ECF) agents and include gadolinium complexes with albumin, polymers, etc.[78] A number of organ-specific contrast agents are also available. Gadolinium-, manganese (Mn^{2+}) - and super-paramagnetic iron oxide (SPIO)-based agents are available for hepatobiliary imaging.[78,80] Ultra-small super-paramagnetic iron oxide (USPIO)- and gadolinium-based agents are available for lymph node and bone marrow imaging.[78] Iron oxide nanoparticles are taken up by the monocyte-macrophage system and can be used as MRI markers of inflammatory and degenerative disorders characterized by enhanced phagocytic activity.[79,80] Mn^{2+}-based agents are particularly useful for neuroimaging.[78] Mn^{2+} can enter the central nervous system neurons

and upon neuronal excitation, gets released into the synaptic cleft. This phenomenon is used to extract information on the axonal transport and trans-synaptic activities. [81,82] (see Figure 3). Orally administered agents are available for gastrointestinal imaging.[78] Oxygen[83] and hyperpolarized gases such as ^{3}He and ^{129}Xe have been employed for pulmonary ventilation studies.[84,85]

A new generation of contrast agents consisting of an assembly of a *contrastophore* conjugate and a target-specific ligand are now being developed for molecular imaging.[79,86] A number of carrier molecules such as antibodies, peptides, polysaccharides, aptamers, and synthetic compounds can be used to deliver the magnetic labels to the specific targets.[79] Tagging of various gadolinium- and nanoparticles-based contrast agents have been performed to monitor the stem cells and immune cells *in vivo*.[87] Investigators have also been able to insert magnetic reporter genes into the cells resulting in expression of iron-storage proteins to be detected on MRI images.[88–90] A group of smart contrast agents, whose relaxivity varies depending upon various local factors such as temperature, pH, redox potential, enzymes, etc. have also been developed.[78,91] Copper-[92] and zinc-responsive[93] contrast agents have also been developed.

Another MRI contrast mechanism, chemical exchange saturation transfer (CEST) originates from the chemical exchange of endogenous amide or hydroxyl protons or from exchangeable sites on exogenous CEST agents.[94] Paramagnetic CEST (PARACEST) and hyperpolarized CEST (hyperCEST) are variations of CEST in which saturation transfer arises from presaturation of exchangeable protons on exogenous paramagnetic or hyperpolarized gas molecules, respectively.[94]

Applications

High-resolution (spatial resolution <100 μm) MRI, also called MR microscopy (MRM) has been performed in small animals (see Figure 4). A desired combination of a number of structural imaging (i.e., $T1$-, $T2$- and spin density-weighted, fat saturated and fluid attenuated, etc.), DTI, perfusion MRI, DCE-MRI, fMRI, and MRS of the region of interest can be performed in a single setting. A broad overview of applications of MRI for animal imaging can be found elsewhere.[80,95–99] MRM provides relatively high-resolution images of brain because of the absence of cardiorespiratory movements.[96] High-field MRM has recently been employed for murine brain imaging at a near single-cell layer resolution (30–40 μm) *in vivo*.[62] DTI with high spatial and angular resolutions has been employed for fiber tractography *in vivo*.[100,101] fMRI has found applications to analyze neuronal activity in normal[102] and diseased rats.[103] Mn^{2+}-enhanced MRI has been employed for neural tract mapping, fMRI, and to investigate neuroarchitecture.[82] Multiparametric MRI including perfusion MRI and diffusion-weighted imaging has been used to investigate small animal stroke models.[104] Perfusion MRI and CE-MRI can be employed to investigate small animal brain tumor models.[105,106]

MRM has also been employed for cardiac,[107] embryonic,[108] and developmental[109] studies. Perfusion fixation can be employed to obtain regional or whole-body high-resolution MRM images.[96] ^{3}He-and ^{129}Xe-enhanced MRM is employed to investigate pulmonary ventilation patterns.[96] Morphologic phenotyping has also been performed by MRM.[96] Longitudinal

MRM studies can be performed to analyze the temporal evaluation of various tumor parameters such as the total volume, vascular permeability, water diffusion and blood oxygenation, etc. Magnetic tagging has been employed to analyze the cellular migration in the brain,[110] heart,[111] liver,[112] and kidneys[113] of small animals *in vivo*. Multiparametric MRI including DTI and perfusion MRI has been used to characterize the rat model of reperfused partial liver infarction[114] and liver tumors.[115,116] DCE-MRI is used to investigate the tumor microvasculature and can potentially be used as an imaging biomarker to measure anti-angiogenic effects of cancer treatments.[68] Affects of interventional procedures such as photodynamic therapy on tumors can also be studied using DCE-MRI (see Figure 5).

Principle applications of MRS are for cancer therapy assessment and analysis of intrinsic metabolic pathways and drug metabolism.[76,99,117] Molecular quantification down to the millimolar range can be performed.[77,99] Because of its ability to detect molecules such as *N*-acetylaspartate, creatine, phosphocreatine, choline, lactate, inositols, alanine, glutamine, and glutamate, ^{1}H MRS has found applications to investigate the molecular pathways *in vivo*.[77] Energy metabolism molecules such as phosphocreatine, adenosine tri-phosphate, phosphorylcholine, and inorganic phosphate (Pi) can be analyzed using ^{31}P-MRS which makes it particularly useful to study tissue energetics.[77] ^{13}C-MRS has relatively lower intrinsic sensitivity and is used to study compounds such as glycogen that are present in a high concentration inside the body.[77] ^{13}C-labeling is employed to study metabolic pathways. ^{17}O-MRS is used to investigate the oxygen metabolism. ^{19}F-MRS is used to investigate ^{19}F-containing drugs such as anesthetic agents, gene activity, pH, metal ion concentrations, oxygen tension, hypoxia, vascular flow, and vascular volume.[118,119] Very high resolution MRS has also recently been performed to investigate the cellular protein content *in vivo*.[120] Further details of various MRS applications can be found elsewhere.[76,99,117]

Challenges and Future Prospects

A very high development and maintenance cost of MRI and NMR scanners restrict their availability; oftentimes *in vivo* animal imaging systems are found in advanced centers only. The desire to obtain very high resolution images using MRM is particularly hindered by a steep reduction in the signal-to-noise ratio with reduced voxel size. The sensitivity of MRI techniques for functional and metabolic measurements is also relatively low when compared to PET and SPECT. Very long image acquisition times for the techniques such as MRS decrease the throughput of the animal research. At last, intrinsic cardiorespiratory movements of the animals are particularly a problem for imaging of the mobile organs.

MRI has an edge over the other imaging techniques because of its ability to provide a multiplicity of information by employing different imaging sequences. This makes MRI a versatile tool to define anatomy and pathophysiology of an animal single-handedly. Recent advances such as availability of MRI scanners with very high magnetic field and gradient strengths, MRI–PET scanners, dedicated small animal imaging microcoils, increased sensitivity of hyperpolarized gas imaging, and faster imaging mechanisms have revolutionized its applications. Development of nanoparticles-based target-specific contrast

agents and innovative contrast mechanisms such as CEST is expected to further take small animal MRI research into a new horizon.

NUCLEAR IMAGING MODALITIES

Two main nuclear imaging modalities namely SPECT and PET are typically used for animal imaging. Dedicated PET[121] and SPECT[122] imaging systems have been developed for small animals. For image acquisition by these modalities, a radionuclide is injected into the body. The radionuclide distributes in the body based on its similarity to other compounds needed by the cells or tissues (e.g., bony phosphates, glucose, water, red blood cells). A SPECT radionuclide undergoes radioactive decay and emits gamma rays of a particular energy. The gamma rays are captured by an external camera to acquire a number of 2D projections from multiple angles which are combined together to form a 3D SPECT image.[123,124] On the other hand, a PET radionuclide undergoes positive beta decay and emits a positron. The positron travels for a short distance (approximately, a few millimeters), annihilates with an electron to emit a pair of photons (energy 511 KeV) that travel nearly 180° apart and are detected by externally placed detectors. The photons coincidently detected by two opposing detectors define a line of response (LOR). The distribution pattern of the LORs is used to reconstruct a 3D image of the radioactivity distribution within the body.[123,124]

Radionuclides and Radiotracers

Extensive information regarding various PET radionuclides can be found elsewhere.[125] Traditional ^{13}N-, ^{11}C-, and ^{15}O-based radionuclides have a very short half-life (i.e., seconds or a few minutes) and can be used at the production site only; their short half-life prevents feasible transport to the remote imaging locations. ^{18}F is the most commonly used PET radionuclid because of its low positron energy, ease of production, and relatively long half-life (50–100 min).[126] Considerable effort has been made to develop nonstandard radionuclides with a long half-life to study time-consuming processes such as protein metabolism and cell proliferation.[126,127] ^{68}Ge and ^{82}Sr, have a relatively long half-life (270.8 and 25.3 days, respectively).[126] Two As isotopes with a long half-life, ^{72}As (26 h) and ^{74}As (17.8 days), are also available.[128,129] The radionuclides can be labeled to a ligand with affinity toward a particular target molecule inside the body for applications such as drug development and to study the pathophysiology of various diseases. Extensive information regarding the process of development and evaluation of a target-specific PET radionuclide can be found elsewhere.[130] 2-Deoxy-2-fluoro-D-glucose (FDG), a glucose analog, is a commonly used ligand.[130–133] Radiolabeled-FDG enters the cells through the glucose transporters and gets phosphorylated by hexokinase. In tissues with low glucose 6-phosphatase, the phosphorylated FDG becomes trapped within the cells. [^{18}F]FDG is the most commonly used agent in PET imaging.[134] Its variant 6-deoxy-6-[^{18}F]fluoro-D-glucose does not undergo intracellular phosphorylation and is used to image glucose transport dynamics[135] (see Figure 6). ^{82}RbCl is a potassium analog that is rapidly taken up by the muscle cells.[136] Na[^{18}F]fluoride is used for bone imaging.[137] Radiolabeled bombesin and its derivatives have been explored for cancer PET imaging.[138] PET radionuclides based upon thymidine kinase pathways, matrix metalloproteases are used for PET imaging of

angiogenesis.[139] Radiolabeled peptide conjugates for PET imaging of apoptosis[140] and tumor protein metabolism[138] have also been developed.

Radiotracers based upon radioactive metals such as ^{99m}Tc, ^{111}In, ^{188}Re, ^{131}I, ^{123}I, ^{201}Th, and ^{133}Xe are often used for SPECT imaging. Specific radiotracers have been developed for SPECT imaging of individual receptors and transport systems in the brain.[141] [^{99m}Tc]-Sestamibi[142] and [^{111}In]-pentetreotide[143] have been employed for myocardial perfusion and neuroendocrine tumor imaging, respectively. 2-Nitroimidazole and nitric oxide derivatives have been used to image tumor hypoxia and inflammation-related changes, respectively.[144] Radiolabeled bombesin and its derivatives have been explored for cancer SPECT imaging.[138] Radiolabeled peptide conjugates for SPECT imaging of apoptosis,[140] amyloid plaques,[145] and tumor protein metabolism[138] have been developed.

Applications

Nuclear imaging modalities can provide quantitative information regarding molecular concentrations by estimating the number of annihilation events or incident gamma photons *in vivo*. The sensitivity of a preclinical PET for the detection of annihilation events is 2–4% and provides images with a spatial resolution of 1–2 mm,[123,146] whereas the sensitivity of a preclinical SPECT is approximately 0.3% and provides images with a spatial resolution of ≈0.5 mm.[123,146] A broad comparative analysis of relative strengths and limitations of SPECT and PET can be found elsewhere.[146,147] PET is 10 times as sensitive as SPECT. On the other hand, availability of large number of radionuclides, simultaneous imaging of multiple agents, cost-effectiveness, and adaptability to specific imaging situations are amongst the few advantages of SPECT. Overall, PET is advantageous over SPECT for drug development and cancer imaging.

PET offers sensitivity in the picomolar range. It has been employed to study myocardial gene expression and effect of its phenotypic expression on the cardiac parameters.[148–150] Cardiac and respiratory gating has also been employed to improve image quality.[150] Neurological applications of PET include monitoring of neurotransmitter function, molecular events in brain tumors, and angiogenic and gene therapies, among others.[148,149] It is employed for tissue characterization, staging, and therapy control in oncology.[148,149,151] Radioarsenic-labeled bavituximab can be used for PET imaging of solid tumor vasculature.[152] Similarly, applications of SPECT have also been described for drug development, and brain and cardiac imaging.[153,154] It has also been used for studies related to gene expression and cancer; however, PET is more preferred nowadays.[153] Bone imaging has also been performed using SPECT. Nuclear imaging modalities have also been employed for imaging of atherosclerotic lesions,[155] amyloid plaques of Alzheimer's disease,[156] and reporter gene imaging.[157] A tumor can be differentiated from inflammation using various proliferation markers.[158] Tumor radiosensitivity can also by monitored by investigating hypoxia and apoptosis.[159]

Challenges and Future Prospects

Although nuclear imaging modalities can be used to reveal molecular events, they are unable to provide any information regarding molecular structures. For characterization of

molecular structures, other techniques such as high performance liquid chromatography (HPLC) need to be used. Further developments in detector technology and image reconstruction algorithms for nuclear imaging modalities are desired to overcome the limitations such as very low detection sensitivities and spatial resolutions. Development of highly target-specific ligands is desired to radiolabel the radionuclides. High costs for PET scanners and short half-life of radionuclides have limited small animal PET imaging to the advanced centers only. Very short half-life of PET radionuclides necessitates the presence of a cyclotron in vicinity of the PET imaging system. Pharmacologic constraints, and prerequisites and interspecies variations in metabolism and mass effects of PET ligands also remain a challenge for extension of results of the animal studies into the clinical practice.[160]

On their positive aspect, nuclear imaging modalities provide a uniform assay system to evaluate pharmacokinetics and pharmacodynamics of the candidate drugs and molecular probes in animal models. Dynamic data acquisition enables complete description of kinetics of new agents in a single animal. Development of new radionuclides and target-specific ligands is likely to play a major role in the understanding of mechanisms of diseases such as myocardial infarction, Parkinson's disease, and Alzheimer's disease and their management.[157] Molecular information from these modalities can be combined with the structural and molecular information provided by CT and MRI. Image registration mechanisms, dual-modality imaging systems, and contrast agents are expected to give promising results in animal imaging as described in Section 'New Frontiers in Multimodality Imaging.'

ULTRASOUND IMAGING

In US imaging, sound waves of a desired frequency (determined by factors including depth of the organ of interest and the desired spatial resolution) are applied from a transducer upon the animal body, a fraction of which gets reflected from the acoustic interfaces (created by difference in stiffness and density variations of the tissues). A part of the reflected waves is detected by the transducer. The intensity pattern of the reflected waves reaching the transducer is used to generate a US image.[161,162] Different US imaging modes such as amplitude and brightness modes can be employed to construct 1D and 2D US images, respectively.[163–165] A number of Doppler US techniques have also been developed in which frequency shift of the sound waves scattered from moving particles (such as blood) is used to determine the velocity of the moving particles.[162,165] Finally, high intensity focused US (HIFU) is a technique in which a high intensity of US is imposed upon the region of interest that results in thermal heating (up to 60°, which leads to coagulation necrosis) and mechanical effects including cavitation and microstreaming at the focal point.[166,167]

Ultrasound Contrast Agents

US contrast agents (UCAs) enhance image contrast by increasing backscatter of the sound waves. Detailed description of physical interactions between the UCAs and various US imaging modes can be found elsewhere.[168,169] A UCA typically consists of a gas core surrounded by a biocompatible stabilizing material such as a protein, lipid, or biopolymer.[169,170] Unfortunately, because of their large size, the UCAs cannot cross from

the vascular pool into the extravascular space and hence have applications for vascular pool imaging only. Nontargeted UCAs have been used as red cell tracers.[171]

Target-specific UCAs are developed by using various strategies such as surface property modifications or covalent linkage of targeting ligands.[172] A number of inflammation-specific UCAs have been developed by targeting the leukocytes or inflammation-specific adhesion molecules.[173] Markers such as vascular endothelial growth factor (VEGF) receptors have been exploited to develop angiogenesis-specific UCAs.[173] Fibrin-[174] and platelet-targeted[175] UCAs have also been developed. Recently, stimulus-responsive UCAs have been developed to increase the blood half-life of a drug as well as for US targeting by incorporating a brush border to the lipid shell that protects the targeting ligands from opsonizing factors in the absence of sound waves. Once the UCA is bound to the target, it can be destroyed allowing for the drug payload to be delivered.[176] The UCAs are a powerful tool for delivery because not only can they be targeted and monitored, but their insonation parameters can also be adjusted to induce oscillations that rupture the UCA, releasing the drug/gene payload.[177–179]

Sonoporation or cellular sonication is a technique that via application of the US in the presence of a UCA, transiently enhances local cell membrane permeability by creating pores in the cell membranes and microvasculature,[173] which makes it a promising tool for image-guided drug and gene delivery into the cytoplasm. Large DNA particles as well as nanospheres of diameters up to 75 nm could enter a cell upon *sonoporation*.[180]

Applications

US using the sound waves of 20–40 MHz can provide images with a spatial resolution as high as 30 μm in small animals.[173] In small animal imaging, the depth of penetration limitations associated with high-frequency US are not as problematic as they would be in human imaging. Molecular imaging of cardiovascular diseases is an established application of US and can also be monitored with contrast-enhanced US. Other pathophysiologic processes that can be monitored with contrast-enhanced US are atherosclerosis, angiogenesis, ischemia, inflammation, and thrombosis.[171,172] For example, ICAM-1 and P-selectin targeted UCAs are used to evaluate transplant rejection and ischemia-induced chest pain, respectively. Atherogenesis-associated inflammatory changes can be exploited to characterize atheromatous plaques by US imaging. VCAM- and lipid-UCAs have been used to identify the atheromatous plaques in their early stages and ischemic-reperfusion injuries, respectively.[171] Platelet- and fibrin-specific UCAs can be used to improve clot visualization.[174,175] Ultrasound-induced increase in tPA activity has been exploited for stroke lysis.[181] Tumor growth and its response to therapy can be monitored using angiogenesis-specific UCAs. Several techniques have been developed to monitor tumor neovascularization using US imaging[182–184] (see Figure 7). US can also be used to differentiate tumor therapy-induced inflammatory changes from the residual tumor by using phosphotidyl serine (PS)-modified UCAs because of increased PS receptors at the inflammation site (see Figure 8). Contrast-enhanced US has also been employed to measure the regional blood flow.[185] Detailed information regarding oncologic applications of HIFU can be found elsewhere.[166] Pulsed-HIFU has been employed for targeted drug

delivery.[186–188] *Sonoporation* provides a safe alternative to viral vectors for delivering the nuclear acid material into a cell.[177–179] *Sonoporation* has also been used to disrupt the blood–brain barrier for more efficient drug delivery to the central nervous system. The increased permeability lasts for approximately 4 h after sonication, and molecules up to 40 kDa can be transferred through the pores.[189–191]

Noncontrast-enhanced US imaging has also found a few applications for small animals. For example, US elastography provides useful information regarding mechanical properties of the tissues and can be used to investigate suspicious mass lesions.[192] Intravascular US elastography has been evaluated for characterization of atherosclerotic plaques and mural thrombi in rabbits.[193] *In vivo* characterization of atherosclerotic plaques have also been performed using US.[194]

Challenges and Future Prospects

Operator dependence and challenges to provide whole-body images are the principle pitfalls of US. UCA applications in drug and gene delivery are limited by their relatively low loading capacity. Various strategies such as the utilization of a polymer shell have been employed to improve their loading capacity.[179] Also, the UCAs are confined to the vascular compartment only and cannot be used for extravascular or intracellular imaging.[173] On the other hand, primary advantage of the UCAs is that the signal generated from contrast-enhanced US will be a true indicator of the vascular bed. Noninvasive targeted drug and gene delivery by US can help in formulating new strategies for administration of drugs that would otherwise have a high incidence of adverse effects. US molecular imaging also has an edge over nuclear imaging techniques because of its relatively high spatial resolution, requirement of very low contrast dose, and absence of ionizing radiation exposure.

OPTICAL IMAGING TECHNIQUES

A number of optical imaging techniques have been developed in which the fundamental concept behind image formation is the detection of a photon emitted from inside the animal body by an external camera. In BLI, the photon is emitted upon metabolization of a substrate by a bioluminescent reporter enzyme.[195,196] In FLI, a fluorophore gets excited by absorbing a photon, and releases another photon of comparatively higher wavelength while returning back to the ground state.[195] OCT is based upon the physical principle similar to that of brightness mode of US imaging except that it uses light photons instead of sound waves.[197]

Optical Reporters

Firefly luciferase (*Photinus pyralis*; FLuc) (half-life $\approx$2 h) is the most widely used reporter enzyme for BLI.[198,199] It catalyzes the formation of a luciferin–ATP complex, which gets oxidized leading to production of a cyclic peroxide compound that eventually becomes high-energy oxyluciferin. Oxyluciferin emits light photons of a broad spectrum (peak λ_{max} ~ 560 nm).[198,199] The light emission peaks $\approx$10–12 min after the luciferin injection and gradually decreases over next 60 min.[200] Various ATP-independent luciferases such as sea pansy *Renilla reniformis* luciferase (RLuc),[201] click beetle *Pyrophorus plagiophthalamus*, and marine copepod *Gaussia princeps* Luciferase (GLuc)[202,203] have also been cloned. As

compared to the firefly luciferase, ATP-independent luciferases can be easily fused with other proteins. However, their limited distribution, rapid kinetics, and higher background noise are a few limitations.[199] Bacterial lux operons encode all proteins required for bioluminescence. Hence, lux operon-expressing bacteria do not require an exogenous substrate to produce light. This fact has been exploited to investigate bacterial pathogenesis; however, attempts to incorporate lux operons into mammalian cells have not been successful yet.[199]

Both endogenous (e.g., hemoglobin or collagen) as well as exogenous molecules can act as flourophores for FLI.[199] An exogenous fluorophore molecule can be an organic dye,[204] a fluorescent gene reporter,[205] a fluorescent protein,[206] or a quantum dot.[207] Recently, smart probes, whose conformation changes upon binding to a target (which increases their fluorescence intensity), have also been developed.[208,209] Fluorescent probes emitting light in the near infrared region (NIR) are now being produced to improve the depth of *in vivo* FLI.[210,211] A number of green fluorescent proteins (GFPs) have been developed, which are useful in studying gene expression and protein interactions.[212–215] In addition, red fluorescent proteins (RFPs) have also been developed.[215] The fluorescent proteins can undergo various changes such as photoactivation, photoconversion, and photoswitching.[215] Various mechanisms have also been described for contrast enhancement in OCT images.[197,216]

Applications

Optical imaging techniques can detect optical reporters in concentrations as low as picomolar to femtomolar ranges.[199] Spatial localization of the optical signal can be performed by using other imaging modalities such as planar X-ray imaging. A broad overview of the applications of BLI for small animal imaging can be found elsewhere.[196] Luciferase complementation can be used to monitor protein interactions and their disruption during intracellular signaling or in response to therapy.[199,217,218] Interactions between drugs and their respective receptors can be studied using luciferase-based novel sensors.[219,220] BLI can be used to study the proteosome function and its response to therapeutic drugs,[221,222] gene expression,[223,224] and for T cell imaging[225] *in vivo*. Dynamic BLI has been employed for tumor drug development to study their effect on the neoplastic cells.[226]

NIR fluorescent probes have been used to detect protease activity *in vivo* and are powerful tools for spatial and temporal analyses of molecular mechanisms of disease activity.[227,228] GFP-FLI can be applied for characterization of spatial and temporal dynamics of gene expression, protein localization, and protein–protein interactions in living cells.[212,213] Fluorescence resonance energy transfer (FRET) is an established technique to study protein–protein interactions.[215] Fluorescence signals from tumors can be quantified (see Figure 9). FLI has also been used to track tumor growth in real time[229,230] to analyze tumor–host interactions and to study the tumor response to therapeutic agents.[231] GFPs and RFPs are particularly useful for labeling of primary and metastatic tumor cells.[231] FLI has several advantages over BLI for tumor imaging.[231] Intravital microscopy can be performed at the single cell level[231,232] and can be used for real-time tracking of tumor angiogenesis *in vivo*.[231] Multiphoton laser scanning microscopy can also be performed to detect tumor

angiogenesis *in vivo* through a window created on the skin surface.[233] *In vivo* stem cell tracking has also been performed using FLI.[234]

OCT has been applied for gastrointestinal, ocular, and skin imaging. However, because of very low depth penetration, its applications are limited to superficial imaging only.[197,235]

Challenges and Future Prospects

Limited depth penetration, restricted image planes, and nonlinear relationships between signal intensity, tissue heterogeneity, and depth are a few limitations of optical imaging techniques. Although these techniques enable detection of molecules in concentrations within femtomolar ranges, the information provided by these techniques is qualitative. The use of GFPs can confound the experimental results by altering the transcription and translation rates of the cells.[236] In addition, the surrounding protein cavity (steric hindrance) can also influence the fluorescence of the fluorophores.[237] The major advantages of optical imaging techniques are their relatively low operational costs, simple imaging procedures, absence of ionization radiation exposure, quick image acquisition, and ability to image multiple animals repetitively over a long period of time. Recent development of fluorophores in the NIR range has allowed for imaging of tissues as deep as 7–14 cm.[238] Intravital microscopy can also be used to image deeper tissues *in vivo*.[231] Multispectral imaging has enabled separation and quantification of multiple fluorophores at the same time.[239] Recent developments in BLI concentrate primarily on creating red-shifted luciferase reporter systems for more efficient light transmission through the tissues. Techniques for real-time BLI of moving rodents[240] and dynamic BLI[226,241] have also been developed in the recent past. Today, optical imaging is transforming the way investigators translate gene and protein expression into real-time events.

NEW FRONTIERS IN MULTIMODALITY IMAGING

In order to synergize the information provided by different kinds of images, images produced by two or more techniques are often combined together. There are two common options for combining the images. The first option is coregistration, or fusion, of images acquired from different imaging systems (e.g., MRI and PET, SPECT, and CT).[242,243] This works well for rigid and relatively immobile organs such as the brain. However, for the thorax, abdomen, and pelvis, where organs are relatively more mobile and deformable, the process of registration of sequentially acquired images becomes more complicated. This leads to the second option: development of new imaging systems for simultaneous or sequential imaging of the same volume with minimal movement.[243] Simultaneous imaging is also important for the analysis of dynamic processes such as contrast enhancement, where sets of information need to be acquired simultaneously at different point of times. Various dedicated dual-modality imaging systems have been designed for small animal imaging. In dedicated SPECT–CT[154] and PET–CT[244] (see Figure 10) systems, structural data from CT images are also used to generate attenuation correction maps for SPECT and PET image reconstruction, respectively. Dedicated SPECT–CT systems have found applications for oncology research,[154] development of radiolabeled nanobodies[245] and gene therapy vectors,[246] and investigation of various disease models.[247] PET–CT is principally employed for oncologic imaging.[248] MRI compatible optical imaging systems have been developed.[249]

Dedicated PET–MRI,[250] SPECT–MRI,[251] and optical-PET[252] systems have also been developed for small animal imaging. PET–MRI imaging would be particularly useful for animal research. It provides an opportunity to combine functional information from PET with anatomical as well as various other kinds of information (i.e., functional, metabolic, or perfusion) from MRI.[253] Multimodality contrast agents are also being developed nowadays which enable analyses of the same event by multiple imaging techniques. A number of dual-modality probes have been described for *in vivo* molecular imaging.[254,255] Multimodal contrast agents have been developed for corroboration of MRI with other modalities.[15,256] A novel triple-modality reporter gene for whole-body fluorescent, bioluminescent, and nuclear imaging have been reported.[257] Synergistically integrated nanoparticles are being projected as an excellent candidate to be multimodal probes for nanobiotechnology.[258]

CONCLUSION

Comparative analyses of the basic principle of image formation, image acquisition times, important applications, strengths, and limitations of the individual imaging techniques can be found elsewhere.[1,2] Maximum spatial resolution, sensitivity, and tissue depth penetration of these techniques have been compared in another review.[258] None of the imaging techniques are free of limitations or serves every purpose of image acquisition from all areas of the animal. PET and SPECT have very high sensitivity, down to picomolar and nanomolar concentrations, respectively. Superb sensitivity enables application of these imaging techniques for quantitative analysis of tumor cell metabolism. Availability of a variety of probes and strategies confer PET a high degree of versatility. The ability to detect multiple probes simultaneously and the availability of radioisotopes with longer half-life are some of advantages of SPECT over PET; however, they are limited in their spatial resolution.

Amongst structural imaging techniques, MRI provides images with high spatial resolution and can provide anatomical, functional, metabolic as well as molecular information in the same setting. Exposure to RF waves and magnetic fields does not affect animal pathophysiology to a significant extent. μCT also provides images with excellent spatial resolution and is particularly useful for imaging of bones and lungs. Although not typically a significant issue in clinical CT imaging, very high X-ray doses required for μCT imaging could decrease the life expectancy and confound the experimental results by altering the pathophysiology of the animals. Ultrasound is more applicable to analyze tissue physiology relatively close to the surface of the live animal in real time. Optical imaging techniques provide molecular sensitivity down to femtomolar ranges. BLI provides a relative measure of cell viability or cell function and has a high throughput. FLI is a versatile method that can perform multiplexed imaging by using multiple reporter wavelengths.[1,2] Tomographic (i.e., image slices) techniques are only now emerging with BLI and FLI. However, low tissue depth penetration and qualitative nature of results are significant drawbacks of optical imaging techniques.

In conclusion, we provided a broad overview of various imaging techniques and their emerging applications for whole animal research. Information provided here is expected to provide an insight into the vast field of whole animal imaging to scientists involved in

translational research. Translational research plays a vital role in translation of scientific research into practical applications (bench-to-bedside) and hence enables development of new techniques for management of human ailments. Overall, *in vivo* biomedical imaging techniques provide an important tool in the armamentarium of biomedical researchers today, and offer great potential for future impact on advancement of human society.

Acknowledgments

References

1. Koo V, Hamilton PW, Williamson K. Non-invasive in vivo imaging in small animal research. Cell Oncol. 2006; 28:127–139. [PubMed: 16988468]

2. Lyons SK. Advances in imaging mouse tumour models *in vivo*. J Pathol. 2005; 205:194–205. [PubMed: 15641018]

3. Ritman EL. Small-animal CT - its difference from, and impact on, clinical CT. Nucl Instrum Methods Phys Res A. 2007; 580:968–970. [PubMed: 18836514]

4. Badea CT, Drangova M, Holdsworth DW, Johnson GA. In vivo small-animal imaging using micro-CT and digital subtraction angiography. Phys Med Biol. 2008; 53:319–350. [PubMed: 18184988]

5. Badea CT, Fubara B, Hedlund LW, Johnson GA. 4-D micro-CT of the mouse heart. Mol Imaging. 2005; 4:110–116. [PubMed: 16105509]

6. Drangova M, Ford NL, Detombe SA, Wheatley AR, Holdsworth DW. Fast retrospectively gated quantitative four-dimensional (4D) cardiac micro computed tomography imaging of free-breathing mice. Invest Radiol. 2007; 42:85–94. [PubMed: 17220726]

7. Badea CT, Hedlund LW, De Lin M, Mackel JS, Samei E, et al. Tomographic digital subtraction angiography for lung perfusion estimation in rodents. Med Phys. 2007; 34:1546–1555. [PubMed: 17555236]

8. Popovtzer R, Agrawal A, Kotov NA, et al. Targeted gold nanoparticles enable molecular CT imaging of cancer. Nano Lett. 2008; 8:4593–4596. [PubMed: 19367807]

9. Weichert JP, Longino MA, Bakan DA, et al. Polyiodinated triglyceride analogs as potential computed tomography imaging agents for the liver. J Med Chem. 1995; 38:636–646. [PubMed: 7861412]

10. Weber SM, Peterson KA, Durkee B, et al. Imaging of murine liver tumor using microCT with a hepatocyte-selective contrast agent: accuracy is dependent on adequate contrast enhancement. J Surg Res. 2004; 119:41–45. [PubMed: 15126080]

11. Badea CT, Hedlund LW, De Lin M, Boslego Mackel JF, Johnson GA. Tumor imaging in small animals with a combined micro-CT/micro-DSA system using iodinated conventional and blood pool contrast agents. Contrast Media Mol Imaging. 2006; 1:153–164. [PubMed: 17193692]

12. Chouker A, Lizak M, Schimel D, et al. Comparison of Fenestra VC Contrast-enhanced computed tomography imaging with gadopentetate dimeglumine and ferucarbotran magnetic resonance imaging for the *in vivo* evaluation of murine liver damage after ischemia and reperfusion. Invest Radiol. 2008; 43:77–91. [PubMed: 18197060]

13. Henning T, Weber AW, Bauer JS, et al. Imaging characteristics of DHOG, a hepatobiliary contrast agent for preclinical microCT in mice. Acad Radiol. 2008; 15:342–349. [PubMed: 18280932]

14. Kattumuri V, Katti K, Bhaskaran S, et al. Gum arabic as a phytochemical construct for the stabilization of gold nanoparticles: *in vivo* pharmacokinetics and X-ray-contrast-imaging studies. Small. 2007; 3:333–341. [PubMed: 17262759]

15. Alric C, Taleb J, Le Duc G, et al. Gadolinium chelate coated gold nanoparticles as contrast agents for both X-ray computed tomography and magnetic resonance imaging. J Am Chem Soc. 2008; 130:5908–5915. [PubMed: 18407638]

16. Cai QY, Kim SH, Choi KS, et al. Colloidal gold nanoparticles as a blood-pool contrast agent for X-ray computed tomography in mice. Invest Radiol. 2007; 42:797–806. [PubMed: 18007151]

17. Rabin O, Manuel Perez J, Grimm J, Wojtkiewicz G, Weissleder R. An X-ray computed tomography imaging agent based on long-circulating bismuth sulphide nanoparticles. Nat Mater. 2006; 5:118–122. [PubMed: 16444262]

18. Mukundan S Jr, Ghaghada KB, Badea CT, et al. A liposomal nanoscale contrast agent for preclinical CT in mice. Am J Roentgenol. 2006; 186:300–307. [PubMed: 16423931]

19. Ferrari M. Cancer nanotechnology: opportunities and challenges. Nat Rev Cancer. 2005; 5:161–171. [PubMed: 15738981]

20. Wyss C, Schaefer SC, Juillerat-Jeanneret L, et al. Molecular imaging by micro-CT: specific E-selectin imaging. Eur Radiol. 2009; 19:2487–2494. [PubMed: 19440717]

21. Friedman PJ, Tisi GM. "Alveolarization" of tantalum powder in experimental bronchography and the clearance of inhaled particles from the lung. Radiology. 1972; 104:523–535. [PubMed: 5051468]

22. Lam WW, Holdsworth DW, Du LY, Drangova M, McCormack DG, et al. Micro-CT imaging of rat lung ventilation using continuous image acquisition during xenon gas contrast enhancement. J Appl Physiol. 2007; 103:1848–1856. [PubMed: 17690202]

23. Badea CT, Schreibmann E, Fox T. A registration based approach for 4D cardiac micro-CT using combined prospective and retrospective gating. Med Phys. 2008; 35:1170–1179. [PubMed: 18491508]

24. Detombe SA, Ford NL, Xiang F, Lu X, Feng Q, et al. Longitudinal follow-up of cardiac structure and functional changes in an infarct mouse model using retrospectively gated micro-computed tomography. Invest Radiol. 2008; 43:520–529. [PubMed: 18580335]

25. Clauss SB, Walker DL, Kirby ML, Schimel D, Lo CW. Patterning of coronary arteries in wildtype and connexin43 knockout mice. Dev Dyn. 2006; 235:2786–2794. [PubMed: 16802337]

26. Badea CT, Bucholz E, Hedlund LW, Rockman HA, Johnson GA. Imaging methods for morphological and functional phenotyping of the rodent heart. Toxicol Pathol. 2006; 34:111–117. [PubMed: 16507552]

27. Walters EB, Panda K, Bankson JA, Brown E, Cody DD. Improved method of *in vivo* respiratory-gated micro-CT imaging. Phys Med Biol. 2004; 49:4163–4172. [PubMed: 15470930]

28. Bolender RP, Hyde DM, Dehoff RT. Lung morphometry: a new generation of tools and experiments for organ, tissue, cell, and molecular biology. Am J Physiol. 1993; 265:521–548.

29. Shofer S, Badea C, Auerbach S, Schwartz DA, Johnson GA. A micro-computed tomography-based method for the measurement of pulmonary compliance in healthy and bleomycin-exposed mice. Exp Lung Res. 2007; 33:169–183. [PubMed: 17558678]

30. Molthen RC, Karau KL, Dawson CA. Quantitative models of the rat pulmonary arterial tree morphometry applied to hypoxia-induced arterial remodeling. J Appl Physiol. 2004; 97:2372–2384. discussion 2354. [PubMed: 15333611]

31. Langheinrich AC, Leithauser B, Greschus S, et al. Acute rat lung injury: feasibility of assessment with micro-CT. Radiology. 2004; 233:165–171. [PubMed: 15317950]

32. Cody DD, Nelson CL, Bradley WM, et al. Murine lung tumor measurement using respiratory-gated micro-computed tomography. Invest Radiol. 2005; 40:263–269. [PubMed: 15829823]

33. Hori Y, Takasuka N, Mutoh M, et al. Periodic analysis of urethane-induced pulmonary tumors in living A/J mice by respiration-gated X-ray microcomputed tomography. Cancer Sci. 2008; 99:1774–1777. [PubMed: 18616525]

34. Postnov AA, Meurrens K, Weiler H, et al. In vivo assessment of emphysema in mice by high resolution X-ray microtomography. J Microsc. 2005; 220:70–75. [PubMed: 16269065]

35. Montet X, Pastor CM, Vallee JP, et al. Improved visualization of vessels and hepatic tumors by microcomputed tomography (CT) using iodinated liposomes. Invest Radiol. 2007; 42:652–658. [PubMed: 17700281]

36. Kim HW, Cai QY, Jun HY, et al. Micro-CT imaging with a hepatocyte-selective contrast agent for detecting liver metastasis in living mice. Acad Radiol. 2008; 15:1282–1290. [PubMed: 18790400]

37. Graham KC, Detombe SA, MacKenzie LT, et al. Contrast-enhanced microcomputed tomography using intraperitoneal contrast injection for the assessment of tumor-burden in liver metastasis models. Invest Radiol. 2008; 43:488–495. [PubMed: 18580331]

38. Wan SY, Ritman EL, Higgins WE. Multi-generational analysis and visualization of the vascular tree in 3D micro-CT images. Comput Biol Med. 2002; 32:55–71. [PubMed: 11879820]

39. Fortepiani LA, Ruiz MC, Passardi F, et al. Effect of losartan on renal microvasculature during chronic inhibition of nitric oxide visualized by micro-CT. Am J Physiol Renal Physiol. 2003; 285:852–860.

40. Ortiz MC, Garcia-Sanz A, Bentley MD, et al. Microcomputed tomography of kidneys following chronic bile duct ligation. Kidney Int. 2000; 58:1632–1640. [PubMed: 11012897]

41. Garcia-Sanz A, Rodriguez-Barbero A, Bentley MD, Ritman EL, Romero JC. Three-dimensional microcomputed tomography of renal vasculature in rats. Hypertension. 1998; 31:440–444. [PubMed: 9453342]

42. Bentley MD, Ortiz MC, Ritman EL, Romero JC. The use of microcomputed tomography to study microvasculature in small rodents. Am J Physiol Regul Integr Comp Physiol. 2002; 282:1267–1279.

43. Bentley MD, Jorgensen SM, Lerman LO, Ritman EL, Romero JC. Visualization of three-dimensional nephron structure with microcomputed tomography. Anat Rec (Hoboken). 2007; 290:277–283. [PubMed: 17525936]

44. David V, Laroche N, Boudignon B, et al. Noninvasive *in vivo* monitoring of bone architecture alterations in hindlimb-unloaded female rats using novel three-dimensional microcomputed tomography. J Bone Miner Res. 2003; 18:1622–1631. [PubMed: 12968671]

45. Peyrin F, Salome M, Cloetens P, Laval-Jeanet AM, Ritman E, et al. Micro-CT examinations of trabecular bone samples at different resolutions: 14, 7 and 2 micron level. Technol Health Care. 1998; 6:391–401. [PubMed: 10100941]

46. Chappard C, Basillais A, Benhamou L, et al. Comparison of synchrotron radiation and conventional x-ray microcomputed tomography for assessing trabecular bone microarchitecture of human femoral heads. Med Phys. 2006; 33:3568–3577. [PubMed: 17022253]

47. Pattijn V, Van Cleynenbreugel T, Vander Sloten J, Van Audekercke R, Van der Perre G, et al. Structural and radiological parameters for the nondestructive characterization of trabecular bone. Ann Biomed Eng. 2001; 29:1064–1073. [PubMed: 11853257]

48. Barou O, Valentin D, Vico L, et al. High-resolution three-dimensional micro-computed tomography detects bone loss and changes in trabecular architecture early: comparison with DEXA and bone histomorphometry in a rat model of disuse osteoporosis. Invest Radiol. 2002; 37:40–46. [PubMed: 11753153]

49. Leander P. A new liposomal contrast medium for CT of the liver. An imaging study in a rabbit tumour model. Acta Radiol. 1996; 37:63–68. [PubMed: 8611327]

50. Fushiki H, Kanoh-Azuma T, Katoh M, et al. Quantification of mouse pulmonary cancer models by microcomputed tomography imaging. Cancer Sci. 2009; 100:1544–1549. [PubMed: 19459854]

51. Kiessling F, Greschus S, Lichy MP, et al. Volumetric computed tomography (VCT): a new technology for noninvasive, high-resolution monitoring of tumor angiogenesis. Nat Med. 2004; 10:1133–1138. [PubMed: 15361864]

52. Choquet P, Calon A, Breton E, et al. Multiple-contrast X-ray micro-CT visualization of colon malformations and tumours in situ in living mice. C R Biol. 2007; 330:821–827. [PubMed: 17923376]

53. Pickhardt PJ, Halberg RB, Taylor AJ, et al. Microcomputed tomography colonography for polyp detection in an in vivo mouse tumor model. Proc Natl Acad Sci U S A. 2005; 102:3419–3422. [PubMed: 15728368]

54. Brown SL, Freytag SO, Barton KN, et al. Reporter gene imaging using radiographic contrast from non-radioactive iodide sequestered by the sodium-iodide symporter. Contrast Media Mol Imaging. 2007; 2:240–247. [PubMed: 18058866]

55. Kobayashi S, Hori M, Dono K, et al. In vivo real-time microangiography of the liver in mice using synchrotron radiation. J Hepatol. 2004; 40:405–408. [PubMed: 15123353]

56. de Lin M, Ning L, Badea CT, Mistry NN, Qi Y, et al. A high-precision contrast injector for small animal x-ray digital subtraction angiography. IEEE Trans Biomed Eng. 2008; 55:1082–1091. [PubMed: 18334400]

57. Siablis D, Liatsikos EN, Karnabatidis D, et al. Digital subtraction angiography and computer assisted image analysis for the evaluation of the antiangiogenetic effect of ionizing radiation on tumor angiogenesis. Int Urol Nephrol. 2006; 38:407–411. [PubMed: 17033888]

58. Ritman EL. Vision 20/20: increased image resolution versus reduced radiation exposure. Med Phys. 2008; 35:2502–2512. [PubMed: 18649483]

59. Badea CT, Wetzel AW, Mistry N, Pomerantz S, Nave D, et al. Left ventricle volume measurements in cardiac micro-CT: the impact of radiation dose and contrast agent. Comput Med Imaging Graph. 2008; 32:239–250. [PubMed: 18243656]

60. Harding G, Kosanetzky J, Neitzel U. X-ray diffraction computed tomography. Med Phys. 1987; 14:515–525. [PubMed: 3626990]

61. Beckmann F, Bonse U, Busch F, Gunnewig O. X-ray microtomography (microCT) using phase contrast for the investigation of organic matter. J Comput Assist Tomogr. 1997; 21:539–553. [PubMed: 9216758]

62. Boretius S, Kasper L, Tammer R, Michaelis T, Frahm J. MRI of cellular layers in mouse brain *in vivo*. Neuroimage. 2009; 47:1252–1260. [PubMed: 19520174]

63. Brockmann MA, Kemmling A, Groden C. Current issues and perspectives in small rodent magnetic resonance imaging using clinical MRI scanners. Methods. 2007; 43:79–87. [PubMed: 17720566]

64. Poirier-Quinot M, Ginefri JC, Girard O, Robert P, Darrasse L. Performance of a miniature high-temperature superconducting (HTS) surface coil for *in vivo* microimaging of the mouse in a standard 1. 5T clinical whole-body scanner. Magn Reson Med. 2008; 60:917–927. [PubMed: 18816812]

65. McGowan JC. Basic principles of magnetic resonance imaging. Neuroimaging Clin N Am. 2008; 18:623–636 x. [PubMed: 19068405]

66. Bitar R, Leung G, Perng R, et al. MR pulse sequences: what every radiologist wants to know but is afraid to ask. Radiographics. 2006; 26:513–537. [PubMed: 16549614]

67. Nitz WR, Reimer P. Contrast mechanisms in MR imaging. Eur Radiol. 1999; 9:1032–1046. [PubMed: 10415233]

68. Hylton N. Dynamic contrast-enhanced magnetic resonance imaging as an imaging biomarker. J Clin Oncol. 2006; 24:3293–3298. [PubMed: 16829653]

69. Keston P, Murray AD, Jackson A. Cerebral perfusion imaging using contrast-enhanced MRI. Clin Radiol. 2003; 58:505–513. [PubMed: 12834633]

70. Ostergaard L. Principles of cerebral perfusion imaging by bolus tracking. J Magn Reson Imaging. 2005; 22:710–717. [PubMed: 16261573]

71. Liu TT, Brown GG. Measurement of cerebral perfusion with arterial spin labeling: part 1. Methods J Int Neuropsychol Soc. 2007; 13:517–525.

72. Van Laar PJ, Van der Grond J, Hendrikse J. Brain perfusion territory imaging: methods and clinical applications of selective arterial spin-labeling MR imaging. Radiology. 2008; 246:354–364. [PubMed: 18227536]

73. Brown GG, Perthen JE, Liu TT, Buxton RB. A primer on functional magnetic resonance imaging. Neuropsychol Rev. 2007; 17:107–125. [PubMed: 17468956]

74. Mukherjee P, Berman JI, Chung SW, Hess CP, Henry RG. Diffusion tensor MR imaging and fiber tractography: theoretic underpinnings. Am J Neuroradiol. 2008; 29:632–641. [PubMed: 18339720]

75. Skoch A, Jiru F, Bunke J. Spectroscopic imaging: basic principles. Eur J Radiol. 2008; 67:230–239. [PubMed: 18434063]

76. Serkova NJ, Hasebroock KM, Kraft SL. Magnetic resonance spectroscopy of living tissues. Methods Mol Biol. 2009; 520:315–327. [PubMed: 19381964]

77. Schaeffter T, Dahnke H. Magnetic resonance imaging and spectroscopy. Handb Exp Pharmacol. 2008; 185:75–90. [PubMed: 18626799]

78. Geraldes CF, Laurent S. Classification and basic properties of contrast agents for magnetic resonance imaging. Contrast Media Mol Imaging. 2009; 4:1–23. [PubMed: 19156706]

79. Burtea C, Laurent S, Vander Elst L, Muller RN. Contrast agents: magnetic resonance. Handb Exp Pharmacol. 2008; 185:135–165. [PubMed: 18626802]

80. Modo M, Hoehn M, Bulte JW. Cellular MR imaging. Mol Imaging. 2005; 4:143–164. [PubMed: 16194447]

81. Leergaard TB, Bjaalie JG, Devor A, Wald LL, Dale AM. In vivo tracing of major rat brain pathways using manganese-enhanced magnetic resonance imaging and three-dimensional digital atlasing. Neuroimage. 2003; 20:1591–1600. [PubMed: 14642470]

82. Silva AC, Bock NA. Manganese-enhanced MRI: an exceptional tool in translational neuroimaging. Schizophr Bull. 2008; 34:595–604. [PubMed: 18550591]

83. Ohno Y, Hatabu H. Basics concepts and clinical applications of oxygen-enhanced MR imaging. Eur J Radiol. 2007; 64:320–328. [PubMed: 17980535]

84. Mai VM. Hyperpolarized gas and oxygen-enhanced magnetic resonance imaging. Methods Mol Med. 2006; 124:325–345. [PubMed: 16506428]

85. McAdams HP, Hatabu H, Donnelly LF, Chen Q, Tadamura E, et al. Novel techniques for MR imaging of pulmonary airspaces. Magn Reson Imaging Clin N Am. 2000; 8:205–219. [PubMed: 10730243]

86. Yang JJ, Yang J, Wei L, et al. Rational design of protein-based MRI contrast agents. J Am Chem Soc. 2008; 130:9260–9267. [PubMed: 18576649]

87. Budde MD, Frank JA. Magnetic tagging of therapeutic cells for MRI. J Nucl Med. 2009; 50:171–174. [PubMed: 19164242]

88. Genove G, DeMarco U, Xu H, Goins WF, Ahrens ET. A new transgene reporter for *in vivo* magnetic resonance imaging. Nat Med. 2005; 11:450–454. [PubMed: 15778721]

89. Cohen B, Ziv K, Plaks V, et al. MRI detection of transcriptional regulation of gene expression in transgenic mice. Nat Med. 2007; 13:498–503. [PubMed: 17351627]

90. Zurkiya O, Chan AW, Hu X. MagA is sufficient for producing magnetic nanoparticles in mammalian cells, making it an MRI reporter. Magn Reson Med. 2008; 59:1225–1231. [PubMed: 18506784]

91. Zhao D, Jiang L, Mason RP. Measuring changes in tumor oxygenation. Methods Enzymol. 2004; 386:378–418. [PubMed: 15120262]

92. Que EL, Gianolio E, Baker SL, Wong AP, Aime S, et al. Copper-responsive magnetic resonance imaging contrast agents. J Am Chem Soc. 2009; 131:8527–8536. [PubMed: 19489557]

93. Major JL, Boiteau RM, Meade TJ. Mechanisms of ZnII-activated magnetic resonance imaging agents. Inorg Chem. 2008; 47:10788–10795. [PubMed: 18928280]

94. Sherry AD, Woods M. Chemical exchange saturation transfer contrast agents for magnetic resonance imaging. Annu Rev Biomed Eng. 2008; 10:391–411. [PubMed: 18647117]

95. Tyszka JM, Fraser SE, Jacobs RE. Magnetic resonance microscopy: recent advances and applications. Curr Opin Biotechnol. 2005; 16:93–99. [PubMed: 15722021]

96. Driehuys B, Nouls J, Badea A, et al. Small animal imaging with magnetic resonance microscopy. Ilar J. 2008; 49:35–53. [PubMed: 18172332]

97. Kiessling F. Noninvasive cell tracking. Handb Exp Pharmacol. 2008; 185:305–321. [PubMed: 18626608]

98. Pirko I, Fricke ST, Johnson AJ, Rodriguez M, Macura SI. Magnetic resonance imaging, microscopy, and spectroscopy of the central nervous system in experimental animals. Neuro Rx. 2005; 2:250–264.

99. Rodriguez I, Perez-Rial S, Gonzalez-Jimenez J, et al. Magnetic resonance methods and applications in pharmaceutical research. J Pharm Sci. 2008; 97:3637–3665. [PubMed: 18228597]

100. Cohen-Adad J, Benali H, Hoge RD, Rossignol S. In vivo DTI of the healthy and injured cat spinal cord at high spatial and angular resolution. Neuroimage. 2008; 40:685–697. [PubMed: 18201909]

101. Asanuma T, Doblas S, Tesiram YA, et al. Diffusion tensor imaging and fiber tractography of C6 rat glioma. J Magn Reson Imaging. 2008; 28:566–573. [PubMed: 18777530]

102. Austin VC, Blamire AM, Grieve SM, et al. Differences in the BOLD fMRI response to direct and indirect cortical stimulation in the rat. Magn Reson Med. 2003; 49:838–847. [PubMed: 12704766]

103. Tenney JR, Duong TQ, King JA, Ferris CF. FMRI of brain activation in a genetic rat model of absence seizures. Epilepsia. 2004; 45:576–582. [PubMed: 15144421]

104. Chen F, Suzuki Y, Nagai N, et al. Rodent stroke induced by photochemical occlusion of proximal middle cerebral artery: evolution monitored with MR imaging and histopathology. Eur J Radiol. 2007; 63:68–75. [PubMed: 17337149]

105. Ulmer S, Reeh M, Krause J, et al. Dynamic contrast-enhanced susceptibility-weighted perfusion MRI (DSC-MRI) in a glioma model of the rat brain using a conventional receive-only surface coil with a inner diameter of 47 mm at a clinical 1. 5 T scanner. J Neurosci Methods. 2008; 172:168–172. [PubMed: 18538856]

106. Claes A, Gambarota G, Hamans B, et al. Magnetic resonance imaging-based detection of glial brain tumors in mice after antiangiogenic treatment. Int J Cancer. 2008; 122:1981–1986. [PubMed: 18081012]

107. Bucholz E, Ghaghada K, Qi Y, Mukundan S, Johnson GA. Four-dimensional MR microscopy of the mouse heart using radial acquisition and liposomal gadolinium contrast agent. Magn Reson Med. 2008; 60:111–118. [PubMed: 18581419]

108. Hogers B, Gross D, Lehmann V, et al. Magnetic resonance microscopy at 17. 6-Tesla on chicken embryos in vitro. J Magn Reson Imaging. 2001; 14:83–86. [PubMed: 11436219]

109. Smith BR. Magnetic resonance microscopy in cardiac development. Microsc Res Tech. 2001; 52:323–330. [PubMed: 11180623]

110. Modo M, Mellodew K, Cash D, et al. Mapping transplanted stem cell migration after a stroke: a serial, *in vivo* magnetic resonance imaging study. Neuroimage. 2004; 21:311–317. [PubMed: 14741669]

111. Hendry SL II, Van der Bogt KE, Sheikh AY, et al. Multimodal evaluation of *in vivo* magnetic resonance imaging of myocardial restoration by mouse embryonic stem cells. J Thorac Cardiovasc Surg. 2008; 136:1028–1037. e1021. [PubMed: 18954646]

112. Evgenov NV, Medarova Z, Pratt J, et al. In vivo imaging of immune rejection in transplanted pancreatic islets. Diabetes. 2006; 55:2419–2428. [PubMed: 16936189]

113. Evgenov NV, Medarova Z, Dai G, Bonner-Weir S, Moore A. In vivo imaging of islet transplantation. Nat Med. 2006; 12:144–148. [PubMed: 16380717]

114. Wu X, Wang H, Chen F, et al. Rat model of reperfused partial liver infarction: characterization with multiparametric magnetic resonance imaging, microangiography, and histomorphology. Acta Radiol. 2009; 50:276–287. [PubMed: 19160078]

115. Wang H, Sun X, Chen F, et al. Treatment of rodent liver tumor with combretastatin a4 phosphate: non-invasive therapeutic evaluation using multiparametric magnetic resonance imaging in correlation with microangiography and histology. Invest Radiol. 2009; 44:44–53. [PubMed: 19034028]

116. Wang H, Van de Putte M, Chen F, et al. Murine liver implantation of radiation-induced fibrosarcoma: characterization with MR imaging, microangiography and histopathology. Eur Radiol. 2008; 18:1422–1430. [PubMed: 18343928]

117. Gillies RJ, Morse DL. In vivo magnetic resonance spectroscopy in cancer. Annu Rev Biomed Eng. 2005; 7:287–326. [PubMed: 16004573]

118. Yu JX, Kodibagkar VD, Cui W, Mason RP. 19F: a versatile reporter for non-invasive physiology and pharmacology using magnetic resonance. Curr Med Chem. 2005; 12:819–848. [PubMed: 15853714]

119. Yu, JX.; Cui, W.; Zhao, D.; Cui, W.; Mason, RP. Non-invasive physiology and pharmacology using 19F magnetic resonance. In: Tressaud, A.; Haufe, G., editors. Flourine and Health. Elsevier Science and Technology; 2008. p. 198-276.

120. Selenko P, Wagner G. Looking into live cells with in-cell NMR spectroscopy. J Struct Biol. 2007; 158:244–253. [PubMed: 17502240]

121. Constantinescu CC, Mukherjee J. Performance evaluation of an Inveon PET preclinical scanner. Phys Med Biol. 2009; 54:2885–2899. [PubMed: 19384008]

122. Mitchell GS, Cherry SR. A high-sensitivity small animal SPECT system. Phys Med Biol. 2009; 54:1291–1305. [PubMed: 19190360]

123. Rowland DJ, Cherry SR. Small-animal preclinical nuclear medicine instrumentation and methodology. Semin Nucl Med. 2008; 38:209–222. [PubMed: 18396180]

124. Cherry, SR.; Sorenson, JA.; Phelps, ME. Physics in Nuclear Medicine. Philadelphia, PA: WB Saunders; 2003.

125. McQuade P, Rowland DJ, Lewis JS, Welch MJ. Positron-emitting isotopes produced on biomedical cyclotrons. Curr Med Chem. 2005; 12:807–818. [PubMed: 15853713]

126. Qaim S. Decay data and production yields of some non-standard positron emitters used in PET. Q J Nucl Med Mol Imaging. 2008; 52:111–120. [PubMed: 18174879]

127. Lewis JS, Welch MJ, Tang L. Workshop on the production, application and clinical translation of "non-standard" PET nuclides: a meeting report. Q J Nucl Med Mol Imaging. 2008; 52:101–106. [PubMed: 18043544]

128. Jennewein M, Hermanne A, Mason RP, Thorpe PE, Rosch F. A new method for the labelling of proteins with radioactive arsenic isotopes. Nucl Instrum Methods Phys Res A. 2006; 569:512–517.

129. Jennewein M, Schmidt A, Novgorodov AF, Qaim SM, Rösch F. A no-carrier-added 72Se/72As radionuclide generator based on distillation. Radiochim Acta. 2004; 92:245–249.

130. Serdons K, Verbruggen A, Bormans GM. Developing new molecular imaging probes for PET. Methods. 2009; 48:104–111. [PubMed: 19318126]

131. Lundqvist H, Tolmachev V. Targeting peptides and positron emission tomography. Biopolymers. 2002; 66:381–392. [PubMed: 12658725]

132. Miller PW, Long NJ, Vilar R, Gee AD. Synthesis of 11C, 18F, 15O, and 13N radiolabels for positron emission tomography. Angew Chem Int Ed Engl. 2008; 47:8998–9033. [PubMed: 18988199]

133. Hutchins GD, Miller MA, Soon VC, Receveur T. Small animal PET imaging. Ilar J. 2008; 49:54–65. [PubMed: 18172333]

134. Aoki J, Inoue T, Tomiyoshi K, et al. Nuclear imaging of bone tumors: FDG-PET. Semin Musculoskelet Radiol. 2001; 5:183–187. [PubMed: 11500164]

135. Landau BR, Spring-Robinson CL, Muzic RF Jr, et al. 6-Fluoro-6-deoxy-D-glucose as a tracer of glucose transport. Am J Physiol Endocrinol Metab. 2007; 293:E237–E245. [PubMed: 17405828]

136. Kaufmann PA. 82-Rubidium—the dawn of cardiac PET in Europe? Eur J Nucl Med Mol Imaging. 2007; 34:1963–1964. [PubMed: 18034240]

137. Grant FD, Fahey FH, Packard AB, Davis RT, Alavi A, et al. Skeletal PET with 18F-fluoride: applying new technology to an old tracer. J Nucl Med. 2008; 49:68–78. [PubMed: 18077529]

138. Smith CJ, Volkert WA, Hoffman TJ. Radiolabeled peptide conjugates for targeting of the bombesin receptor superfamily subtypes. Nucl Med Biol. 2005; 32:733–740. [PubMed: 16243649]

139. Laking GR, Price PM. Positron emission tomographic imaging of angiogenesis and vascular function. Br J Radiol. 2003; 76:S50–S59. [PubMed: 15456714]

140. Lahorte CM, Vanderheyden JL, Steinmetz N, Van de Wiele C, Dierckx RA, et al. Apoptosis-detecting radioligands: current state of the art and future perspectives. Eur J Nucl Med Mol Imaging. 2004; 31:887–919. [PubMed: 15138718]

141. Kung HF, Kung MP, Choi SR. Radiopharmaceuticals for single-photon emission computed tomography brain imaging. Semin Nucl Med. 2003; 33:2–13. [PubMed: 12605353]

142. Prvulovich E. Myocardial perfusion scintigraphy. Clin Med. 2006; 6:263–266. [PubMed: 16826859]

143. de Herder WW, Kwekkeboom DJ, Valkema R, et al. Neuroendocrine tumors and somatostatin: imaging techniques. J Endocrinol Invest. 2005; 28:132–136. [PubMed: 16625862]

144. De Ridder M, Van Esch G, Engels B, Verovski V, Storme G. Hypoxic tumor cell radiosensitization: role of the iNOS/NO pathway. Bull Cancer. 2008; 95:282–291. [PubMed: 18390408]

145. Kung MP, Zhuang ZP, Hou C, Kung HF. Development and evaluation of iodinated tracers targeting amyloid plaques for SPECT imaging. J Mol Neurosci. 2004; 24:49–53. [PubMed: 15314249]

146. Jansen FP, Vanderheyden JL. The future of SPECT in a time of PET. Nucl Med Biol. 2007; 34:733–735. [PubMed: 17921025]

147. Rahmim A, Zaidi H. PET versus SPECT: strengths, limitations and challenges. Nucl Med Commun. 2008; 29:193–207. [PubMed: 18349789]

148. Riemann B, Schafers KP, Schober O, Schafers M. Small animal PET in preclinical studies: opportunities and challenges. Q J Nucl Med Mol Imaging. 2008; 52:215–221. [PubMed: 18551093]

149. Chatziioannou AF. Molecular imaging of small animals with dedicated PET tomographs. Eur J Nucl Med Mol Imaging. 2002; 29:98–114. [PubMed: 11807613]

150. Yang Y, Rendig S, Siegel S, Newport DF, Cherry SR. Cardiac PET imaging in mice with simultaneous cardiac and respiratory gating. Phys Med Biol. 2005; 50:2979–2989. [PubMed: 15972975]

151. Reske SN, Kotzerke J. FDG-PET for clinical use. Results of the 3rd German Interdisciplinary Consensus Conference, "Onko-PET III", 21 July and 19 September 2000. Eur J Nucl Med. 2001; 28:1707–1723. [PubMed: 11702115]

152. Jennewein M, Lewis MA, Zhao D, et al. Vascular imaging of solid tumors in rats with a radioactive arsenic-labeled antibody that binds exposed phosphatidylserine. Clin Cancer Res. 2008; 14:1377–1385. [PubMed: 18316558]

153. Acton PD, Kung HF. Small animal imaging with high resolution single photon emission tomography. Nucl Med Biol. 2003; 30:889–895. [PubMed: 14698793]

154. Franc BL, Acton PD, Mari C, Hasegawa BH. Small-animal SPECT and SPECT/CT: important tools for preclinical investigation. J Nucl Med. 2008; 49:1651–1663. [PubMed: 18794275]

155. Schillaci O, Danieli R, Padovano F, Testa A, Simonetti G. Molecular imaging of atheroslerotic plaque with nuclear medicine techniques. Int J Mol Med. 2008; 22:3–7. [PubMed: 18575769]

156. Mathis CA, Wang Y, Klunk WE. Imaging beta-amyloid plaques and neurofibrillary tangles in the aging human brain. Curr Pharm Des. 2004; 10:1469–1492. [PubMed: 15134570]

157. Acton PD, Zhou R. Imaging reporter genes for cell tracking with PET and SPECT. Q J Nucl Med Mol Imaging. 2005; 49:349–360. [PubMed: 16407818]

158. Van Waarde A, Elsinga PH. Proliferation markers for the differential diagnosis of tumor and inflammation. Curr Pharm Des. 2008; 14:3326–3339. [PubMed: 19075707]

159. Belkacemi Y, Tsoutsou P, Magne N, Castadot P, Azria D. Metabolic functional imaging for tumor radiosensitivity monitoring. Crit Rev Oncol Hematol. 2007; 62:227–239. [PubMed: 17241788]

160. Ametamey SM, Honer M. Pharmacological prerequisites for PET ligands and practical issues in preclinical PET research. Ernst Schering Res Found Workshop. 2007:317–327. [PubMed: 17172161]

161. Smith J, Finnoff JT. Diagnostic and interventional musculoskeletal ultrasound: part 1. Fundamentals PM R. 2009; 1:64–75.

162. Case TD. Ultrasound physics and instrumentation. Surg Clin North Am. 1998; 78:197–217. [PubMed: 9602843]

163. Rallan D, Harland CC. Ultrasound in dermatology—basic principles and applications. Clin Exp Dermatol. 2003; 28:632–638. [PubMed: 14616832]

164. Coatney RW. Ultrasound imaging: principles and applications in rodent research. Ilar J. 2001; 42:233–247. [PubMed: 11406722]

165. Lawrence JP. Physics and instrumentation of ultrasound. Crit Care Med. 2007; 35:S314–S322. [PubMed: 17667455]

166. Dubinsky TJ, Cuevas C, Dighe MK, Kolokythas O, Hwang JH. High-intensity focused ultrasound: current potential and oncologic applications. Am J Roentgenol. 2008; 190:191–199. [PubMed: 18094311]

167. Haar GT, Coussios C. High intensity focused ultrasound: physical principles and devices. Int J Hyperthermia. 2007; 23:89–104. [PubMed: 17578335]

168. Frinking PJ, Bouakaz A, Kirkhorn J, Ten Cate FJ, de Jong N. Ultrasound contrast imaging: current and new potential methods. Ultrasound Med Biol. 2000; 26:965–975. [PubMed: 10996696]

169. Qin S, Caskey CF, Ferrara KW. Ultrasound contrast microbubbles in imaging and therapy: physical principles and engineering. Phys Med Biol. 2009; 54:R27–R57. [PubMed: 19229096]

170. Quaia E. Microbubble ultrasound contrast agents: an update. Eur Radiol. 2007; 17:1995–2008. [PubMed: 17351779]

171. Villanueva FS. Molecular imaging of cardiovascular disease using ultrasound. J Nucl Cardiol. 2008; 15:576–586. [PubMed: 18674725]

172. Piedra M, Allroggen A, Lindner JR. Molecular imaging with targeted contrast ultrasound. Cerebrovasc Dis. 2009; 27(suppl 2):66–74. [PubMed: 19372662]

173. Schneider M. Molecular imaging and ultrasound-assisted drug delivery. J Endourol. 2008; 22:795–802. [PubMed: 18366315]

174. Klegerman ME, Zou Y, McPherson DD. Fibrin targeting of echogenic liposomes with inactivated tissue plasminogen activator. J Liposome Res. 2008; 18:95–112. [PubMed: 18569446]

175. Martin M, Chung E, Goodall A, et al. Enhanced detection of thromboemboli with the use of targeted microbubbles. Stroke. 2007; 38:2726–2732. [PubMed: 17823379]

176. Borden MA, Zhang H, Gillies RJ, Dayton PA, Ferrara KW. A stimulus-responsive contrast agent for ultrasound molecular imaging. Biomaterials. 2008; 29:597–606. [PubMed: 17977595]

177. Wang, B.; Siahaan, T.; Soltero, R. Drug Delivery: Principles and Applications. New York: Wiley; 2005.

178. Sboros V. Response of contrast agents to ultrasound. Adv Drug Deliv Rev. 2008; 60:1117–1136. [PubMed: 18486270]

179. Tinkov S, Bekeredjian R, Winter G, Coester C. Microbubbles as ultrasound triggered drug carriers. J Pharm Sci. 2009; 98:1935–1961. [PubMed: 18979536]

180. Mehier-Humbert S, Bettinger T, Yan F, Guy RH. Plasma membrane poration induced by ultrasound exposure: implication for drug delivery. J Control Release. 2005; 104:213–222. [PubMed: 15866347]

181. Alexandrov AV. Ultrasound enhanced thrombolysis for stroke. Int J Stroke. 2006; 1:26–29. [PubMed: 18706065]

182. Rychak JJ, Graba J, Cheung AM, et al. Microultrasound molecular imaging of vascular endothelial growth factor receptor 2 in a mouse model of tumor angiogenesis. Mol Imaging. 2007; 6:289–296. [PubMed: 18092513]

183. Korpanty G, Carbon JG, Grayburn PA, Fleming JB, Brekken RA. Monitoring response to anticancer therapy by targeting microbubbles to tumor vasculature. Clin Cancer Res. 2007; 13:323–330. [PubMed: 17200371]

184. Willmann JK, Lutz AM, Paulmurugan R, et al. Dual-targeted contrast agent for US assessment of tumor angiogenesis in vivo. Radiology. 2008; 248:936–944. [PubMed: 18710985]

185. Sullivan JC, Wang B, Boesen EI, D'Angelo G, Pollock JS, Pollock DM. Novel use of ultrasound to examine regional blood flow in the mouse kidney. Am J Physiol Renal Physiol. 2009; 297:F228–F235. [PubMed: 19420115]

186. Dromi S, Frenkel V, Luk A, et al. Pulsed-high intensity focused ultrasound and low temperature-sensitive liposomes for enhanced targeted drug delivery and antitumor effect. Clin Cancer Res. 2007; 13:2722–2727. [PubMed: 17473205]

187. O'Neill BE, Vo H, Angstadt M, Li KP, Quinn T, Frenkel V. Pulsed high intensity focused ultrasound mediated nanoparticle delivery: mechanisms and efficacy in murine muscle. Ultrasound Med Biol. 2009; 35:416–424. [PubMed: 19081668]

188. Hancock HA, Smith LH, Cuesta J, et al. Investigations into pulsed high-intensity focused ultrasound-enhanced delivery: preliminary evidence for a novel mechanism. Ultrasound Med Biol. 2009 Epub ahead of print.

189. Vykhodtseva N, McDannold N, Hynynen K. Progress and problems in the application of focused ultrasound for blood-brain barrier disruption. Ultrasonics. 2008; 48:279–296. [PubMed: 18511095]

190. Raymond SB, Treat LH, Dewey JD, McDannold NJ, Hynynen K, et al. Ultrasound enhanced delivery of molecular imaging and therapeutic agents in Alzheimer's disease mouse models. PLoS ONE. 2008; 3:e2175. [PubMed: 18478109]

191. Sheikov N, McDannold N, Sharma S, Hynynen K. Effect of focused ultrasound applied with an ultrasound contrast agent on the tight junctional integrity of the brain microvascular endothelium. Ultrasound Med Biol. 2008; 34:1093–1104. [PubMed: 18378064]

192. Zhi H, Xiao XY, Yang HY, et al. Semi-quantitating stiffness of breast solid lesions in ultrasonic elastography. Acad Radiol. 2008; 15:1347–1353. [PubMed: 18995186]

193. Maurice RL, Fromageau J, Cardinal MH, et al. Characterization of atherosclerotic plaques and mural thrombi with intravascular ultrasound elastography: a potential method evaluated in an aortic rabbit model and a human coronary artery. IEEE Trans Inf Technol Biomed. 2008; 12:290–298. [PubMed: 18693496]

194. Van Herck J, De Meyer G, Ennekens G, Van Herck P, Herman A, et al. Validation of *in vivo* plaque characterisation by virtual histology in a rabbit model of atherosclerosis. EuroIntervention. 2009; 5:149–156. [PubMed: 19577997]

195. Schulz RB, Semmler W. Fundamentals of optical imaging. Handb Exp Pharmacol. 2008:3–22. [PubMed: 18626796]

196. Zinn KR, Chaudhuri TR, Szafran AA, et al. Noninvasive bioluminescence imaging in small animals. Ilar J. 2008; 49:103–115. [PubMed: 18172337]

197. Testoni PA. Optical coherence tomography. Scientific-World Journal. 2007; 7:87–108. [PubMed: 17334603]

198. de Wet JR, Wood KV, Helinski DR, DeLuca M. Cloning of firefly luciferase cDNA and the expression of active luciferase in Escherichia coli. Proc Natl Acad Sci U S A. 1985; 82:7870–7873. [PubMed: 3906652]

199. Luker GD, Luker KE. Optical imaging: current applications and future directions. J Nucl Med. 2008; 49:1–4. [PubMed: 18077528]

200. Paroo Z, Bollinger RA, Braasch DA, et al. Validating bioluminescence imaging as a high-throughput, quantitative modality for assessing tumor burden. Mol Imaging. 2004; 3:117–124. [PubMed: 15296676]

201. Lorenz WW, McCann RO, Longiaru M, Cormier MJ. Isolation and expression of a cDNA encoding Renilla reniformis luciferase. Proc Natl Acad Sci U S A. 1991; 88:4438–4442. [PubMed: 1674607]

202. Venisnik KM, Olafsen T, Gambhir SS, Wu AM. Fusion of Gaussia luciferase to an engineered anti-carcinoembryonic antigen (CEA) antibody for *in vivo* optical imaging. Mol Imaging Biol. 2007; 9:267–277. [PubMed: 17577599]

203. Tannous BA, Kim DE, Fernandez JL, Weissleder R, Breakefield XO. Codon-optimized Gaussia luciferase cDNA for mammalian gene expression in culture and *in vivo*. Mol Ther. 2005; 11:435–443. [PubMed: 15727940]

204. Kalchenko V, Shivtiel S, Malina V, et al. Use of lipophilic near-infrared dye in whole-body optical imaging of hematopoietic cell homing. J Biomed Opt. 2006; 11:050507. [PubMed: 17092148]

205. Contag CH, Jenkins D, Contag PR, Negrin RS. Use of reporter genes for optical measurements of neoplastic disease in vivo. Neoplasia. 2000; 2:41–52. [PubMed: 10933067]

206. Shcherbo D, Merzlyak EM, Chepurnykh TV, et al. Bright far-red fluorescent protein for whole-body imaging. Nat Methods. 2007; 4:741–746. [PubMed: 17721542]

207. Choi HS, Ipe BI, Misra P, Lee JH, Bawendi MG, et al. Tissue- and organ-selective biodistribution of NIR fluorescent quantum dots. Nano Lett. 2009; 9:2354–2359. [PubMed: 19422261]

208. Morimoto S. In-vivo imaging of tumors with protease activated near-infrared fluorescent probes. Tanpakushitsu Kakusan Koso. 2007; 52:1774–1775. [PubMed: 18051420]

209. Alencar H, Funovics MA, Figueiredo J, Sawaya H, Weissleder R, et al. Colonic adenocarcinomas: near-infrared microcatheter imaging of smart probes for early detection–study in mice. Radiology. 2007; 244:232–238. [PubMed: 17507718]

210. Shaner NC, Steinbach PA, Tsien RY. A guide to choosing fluorescent proteins. Nat Methods. 2005; 2:905–909. [PubMed: 16299475]

211. Klohs J, Wunder A, Licha K. Near-infrared fluorescent probes for imaging vascular pathophysiology. Basic Res Cardiol. 2008; 103:144–151. [PubMed: 18324370]

212. Southward CM, Surette MG. The dynamic microbe: green fluorescent protein brings bacteria to light. Mol Microbiol. 2002; 45:1191–1196. [PubMed: 12207688]

213. Chudakov DM, Lukyanov S, Lukyanov KA. Fluorescent proteins as a toolkit for *in vivo* imaging. Trends Biotechnol. 2005; 23:605–613. [PubMed: 16269193]

214. Hadjantonakis AK, Nagy A. The color of mice: in the light of GFP-variant reporters. Histochem Cell Biol. 2001; 115:49–58. [PubMed: 11219608]

215. Muller-Taubenberger A, Anderson KI. Recent advances using green and red fluorescent protein variants. Appl Microbiol Biotechnol. 2007; 77:1–12. [PubMed: 17704916]

216. Yang C. Molecular contrast optical coherence tomography: a review. Photochem Photobiol. 2005; 81:215–237. [PubMed: 15588122]

217. Luker KE, Smith MC, Luker GD, Gammon ST, Piwnica-Worms H, et al. Kinetics of regulated protein-protein interactions revealed with firefly luciferase complementation imaging in cells and living animals. Proc Natl Acad Sci U S A. 2004; 101:12288–12293. [PubMed: 15284440]

218. Paulmurugan R, Gambhir SS. Novel fusion protein approach for efficient high-throughput screening of small molecule-mediating protein-protein interactions in cells and living animals. Cancer Res. 2005; 65:7413–7420. [PubMed: 16103094]

219. Paulmurugan R, Gambhir SS. An intramolecular folding sensor for imaging estrogen receptor-ligand interactions. Proc Natl Acad Sci U S A. 2006; 103:15883–15888. [PubMed: 17043219]

220. Zhang L, Lee KC, Bhojani MS, et al. Molecular imaging of Akt kinase activity. Nat Med. 2007; 13:1114–1119. [PubMed: 17694068]

221. Luker GD, Pica CM, Song J, Luker KE, Piwnica-Worms D. Imaging 26S proteasome activity and inhibition in living mice. Nat Med. 2003; 9:969–973. [PubMed: 12819780]

222. Safran M, Kim WY, O'Connell F, et al. Mouse model for noninvasive imaging of HIF prolyl hydroxylase activity: assessment of an oral agent that stimulates erythropoietin production. Proc Natl Acad Sci U S A. 2006; 103:105–110. [PubMed: 16373502]

223. Wilsbacher LD, Yamazaki S, Herzog ED, et al. Photic and circadian expression of luciferase in mPeriod1-luc transgenic mice *in vivo*. Proc Natl Acad Sci U S A. 2002; 99:489–494. [PubMed: 11752392]

224. Sadikot RT, Blackwell TS. Bioluminescence: imaging modality for *in vitro* and *in vivo* gene expression. Methods Mol Biol. 2008; 477:383–394. [PubMed: 19082962]

225. Santos EB, Yeh R, Lee J, et al. Sensitive *in vivo* imaging of T cells using a membrane-bound Gaussia princeps luciferase. Nat Med. 2009; 15:338–344. [PubMed: 19219023]

226. Zhao D, Richer E, Antich PP, Mason RP. Antivascular effects of combretastatin A4 phosphate in breast cancer xenograft assessed using dynamic bioluminescence imaging and confirmed by MRI. FASEB J. 2008; 22:2445–2451. [PubMed: 18263704]

227. Funovics M, Weissleder R, Tung CH. Protease sensors for bioimaging. Anal Bioanal Chem. 2003; 377:956–963. [PubMed: 12955390]

228. Grimm J, Kirsch DG, Windsor SD, et al. Use of gene expression profiling to direct in vivo molecular imaging of lung cancer. Proc Natl Acad Sci U S A. 2005; 102:14404–14409. [PubMed: 16183744]

229. Hama Y, Urano Y, Koyama Y, Choyke PL, Kobayashi H. Activatable fluorescent molecular imaging of peritoneal metastases following pretargeting with a biotinylated monoclonal antibody. Cancer Res. 2007; 67:3809–3817. [PubMed: 17440095]

230. Veiseh M, Gabikian P, Bahrami SB, et al. Tumor paint: a chlorotoxin:Cy5. 5 bioconjugate for intraoperative visualization of cancer foci. Cancer Res. 2007; 67:6882–6888. [PubMed: 17638899]

231. Hoffman RM. The multiple uses of fluorescent proteins to visualize cancer *in vivo*. Nat Rev Cancer. 2005; 5:796–806. [PubMed: 16195751]

232. Jain RK, Munn LL, Fukumura D. Dissecting tumour pathophysiology using intravital microscopy. Nat Rev Cancer. 2002; 2:266–276. [PubMed: 12001988]

233. Brown EB, Campbell RB, Tsuzuki Y, et al. In vivo measurement of gene expression, angiogenesis and physiological function in tumors using multiphoton laser scanning microscopy. Nat Med. 2001; 7:864–868. [PubMed: 11433354]

234. Boddington S, Henning TD, Sutton EJ, Daldrup-Link HE. Labeling stem cells with fluorescent dyes for non-invasive detection with optical imaging. J Vis Exp. 2008; 14:3791/686.

235. Fujimoto JG. Optical coherence tomography for ultra-high resolution in vivo imaging. Nat Biotechnol. 2003; 21:1361–1367. [PubMed: 14595364]

236. Sacchetti A, Ciccocioppo R, Alberti S. The molecular determinants of the efficiency of green fluorescent protein mutants. Histol Histopathol. 2000; 15:101–107. [PubMed: 10668201]

237. Maddalo SL, Zimmer M. The role of the protein matrix in green fluorescent protein fluorescence. Photochem Photobiol. 2006; 82:367–372. [PubMed: 16613487]

238. Weissleder R, Ntziachristos V. Shedding light onto live molecular targets. Nat Med. 2003; 9:123–128. [PubMed: 12514725]

239. Levenson RM, Lynch DT, Kobayashi H, Backer JM, Backer MV. Multiplexing with multispectral imaging: from mice to microscopy. Ilar J. 2008; 49:78–88. [PubMed: 18172335]

240. Roncali E, Savinaud M, Levrey O, Rogers KL, Maitrejean S, et al. New device for real-time bioluminescence imaging in moving rodents. J Biomed Opt. 2008; 13:054035. [PubMed: 19021415]

241. Hillman EM, Moore A. All-optical anatomical co-registration for molecular imaging of small animals using dynamic contrast. Nat Photonics. 2007; 1:526–530. [PubMed: 18974848]

242. Zanzonico PB, Nehmeh SA. Introduction to clinical and laboratory (small-animal) image registration and fusion. Conf Proc IEEE Eng Med Biol Soc. 2006; 1:1580–1583. [PubMed: 17946907]

243. Townsend DW. Dual-modality imaging: combining anatomy and function. J Nucl Med. 2008; 49:938–955. [PubMed: 18483101]

244. Liang H, Yang Y, Yang K, Wu Y, Boone JM, et al. A microPET/CT system for in vivo small animal imaging. Phys Med Biol. 2007; 52:3881–3894. [PubMed: 17664583]

245. Gainkam LO, Huang L, Caveliers V, et al. Comparison of the biodistribution and tumor targeting of two 99mTc-labeled anti-EGFR nanobodies in mice, using pinhole SPECT/micro-CT. J Nucl Med. 2008; 49:788–795. [PubMed: 18413403]

246. Raty JK, Liimatainen T, Huhtala T, et al. SPECT/CT imaging of baculovirus biodistribution in rat. Gene Ther. 2007; 14:930–938. [PubMed: 17410181]

247. Wietholt C, Roerig DL, Gordon JB, Haworth ST, Molthen RC, et al. Bronchial circulation angiogenesis in the rat quantified with SPECT and micro-CT. Eur J Nucl Med Mol Imaging. 2008; 35:1124–1132. [PubMed: 18247028]

248. Seemann MD, Beck R, Ziegler S. In vivo tumor imaging in mice using a state-of-the-art clinical PET/CT in comparison with a small animal PET and a small animal CT. Technol Cancer Res Treat. 2006; 5:537–542. [PubMed: 16981797]

249. Allard M, Cote D, Davidson L, Dazai J, Henkelman RM. Combined magnetic resonance and bioluminescence imaging of live mice. J Biomed Opt. 2007; 12:034018. [PubMed: 17614726]

250. Judenhofer MS, Wehrl HF, Newport DF, et al. Simultaneous PET-MRI: a new approach for functional and morphological imaging. Nat Med. 2008; 14:459–465. [PubMed: 18376410]

251. Goetz C, Breton E, Choquet P, Israel-Jost V, et al. SPECT low-field MRI system for small-animal imaging. J Nucl Med. 2008; 49:88–93. [PubMed: 18077535]

252. Alexandrakis G, Rannou FR, Chatziioannou AF. Effect of optical property estimation accuracy on tomographic bioluminescence imaging: simulation of a combined optical-PET (OPET) system. Phys Med Biol. 2006; 51:2045–2053. [PubMed: 16585844]

253. Wehrl HF, Judenhofer MS, Wiehr S, Pichler BJ. Preclinical PET/MR: technological advances and new perspectives in biomedical research. Eur J Nucl Med Mol Imaging. 2009; 36(suppl 1):S56–S68. [PubMed: 19194703]

254. Lee S, Chen X. Dual-modality probes for *in vivo* molecular imaging. Mol Imaging. 2009; 8:87–100. [PubMed: 19397854]

255. Jennings LE, Long NJ. Two is better than one'—probes for dual-modality molecular imaging. Chem Commun (Camb). 2009:3511–3524. [PubMed: 19521594]

256. Daldrup-Link HE, Rudelius M, Metz S, et al. Cell tracking with gadophrin-2: a bifunctional contrast agent for MR imaging, optical imaging, and fluorescence microscopy. Eur J Nucl Med Mol Imaging. 2004; 31:1312–1321. [PubMed: 15138719]

257. Ponomarev V, Doubrovin M, Serganova I, et al. A novel triple-modality reporter gene for whole-body fluorescent, bioluminescent, and nuclear noninvasive imaging. Eur J Nucl Med Mol Imaging. 2004; 31:740–751. [PubMed: 15014901]

258. Cheon J, Lee JH. Synergistically integrated nanoparticles as multimodal probes for nanobiotechnology. Acc Chem Res. 2008; 41:1630–1640. [PubMed: 18698851]

259. Goertzen AL, Meadors AK, Silverman RW, Cherry SR. Simultaneous molecular and anatomic imaging of the mouse in vivo. Phys Med Biol. 2002; 47:4315–4328. [PubMed: 12539974]
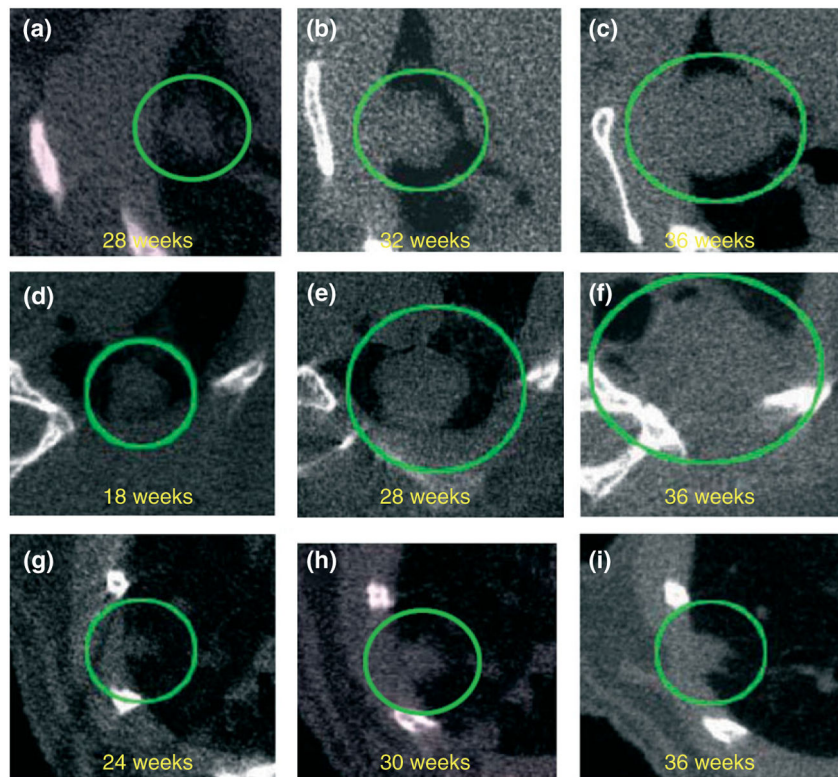
FIGURE 1.
Virtual *in vivo* μCT images of growing lung tumors. Axial microcomputed tomogram (μCT) images of the thorax of a mouse at the indicated time points are shown. μCT images of two lung adenocarcinomas (a–c) and (d–f) and a lung adenoma (g–i) acquired at different ages. Tumors observed in the lung are circled. (Image reproduced with permission from Ref 33. Copyright 2008 Wiley-Blackwell).
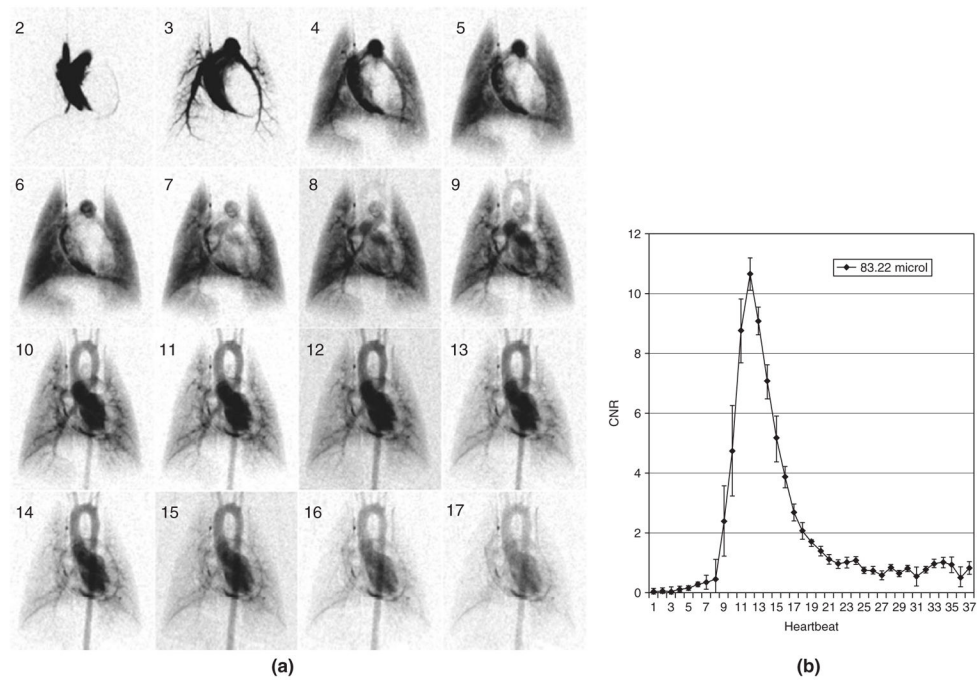
FIGURE 2.
Sixteen successive images (starting at second heartbeat post-injection) from a digital
subtraction angiography (DSA) sequence with a 100 ms contrast injection (**A**). The
reproducibility for ($n = 5$) 100 ms injections (volume injected 83.22 μL) is shown by mean
and standard error at each heartbeat (**B**) in a region of the aortic arch. Note that mean peak
value of contrast-to-noise ratio (CNR) is 10. (Image reproduced with permission from Ref 7.
Copyright 2007).
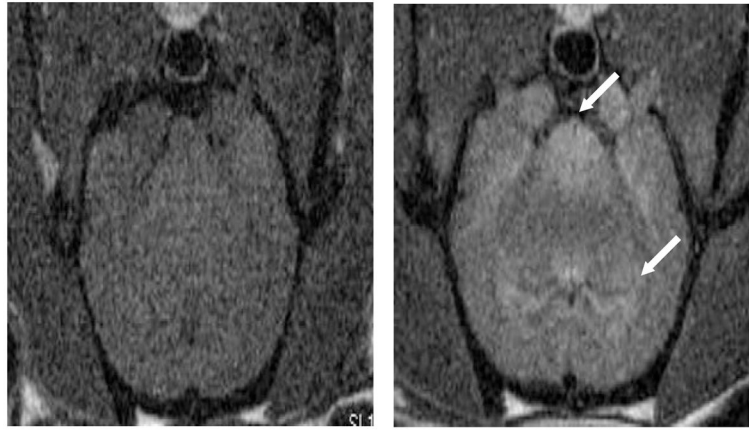
FIGURE 3.
Axial magnetic resonance images of a normal adult male rat brain acquired before (left) and 24 h after (right) intraperitoneal injection of 45 mg/kg $MnCl_2$. $MnCl_2$ results in regions enhancement (arrows). Images were acquired with a conventional T1-weighted spin echo acquisition ($TR/TE = 600/10$ ms) at 7T.
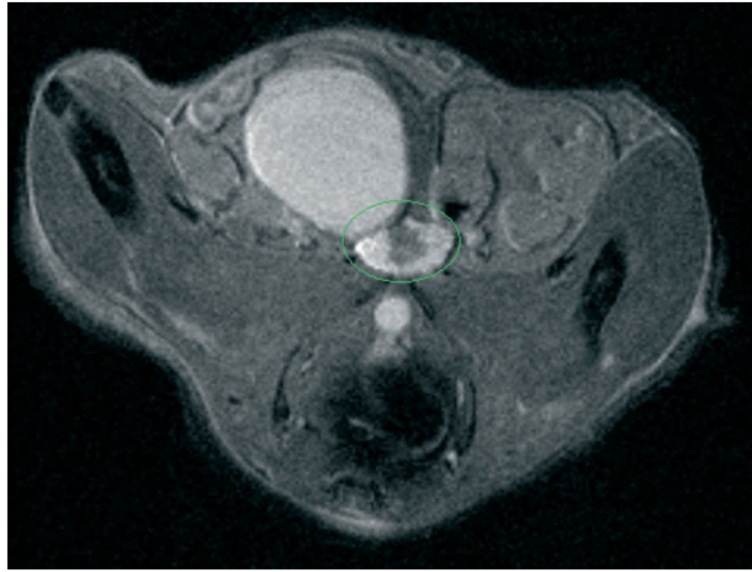
FIGURE 4.
High-resolution (500 × 100 × 100 μm) axial magnetic resonance imaging (MRI) image of dorsolateral prostate of transgenic mouse prone to prostate hyperplasia. Prostate region is outlined in green. The image was acquired by using rapid acquisition with refocused echoes (RARE) sequence (*TR/TE* = 5000/15 ms).
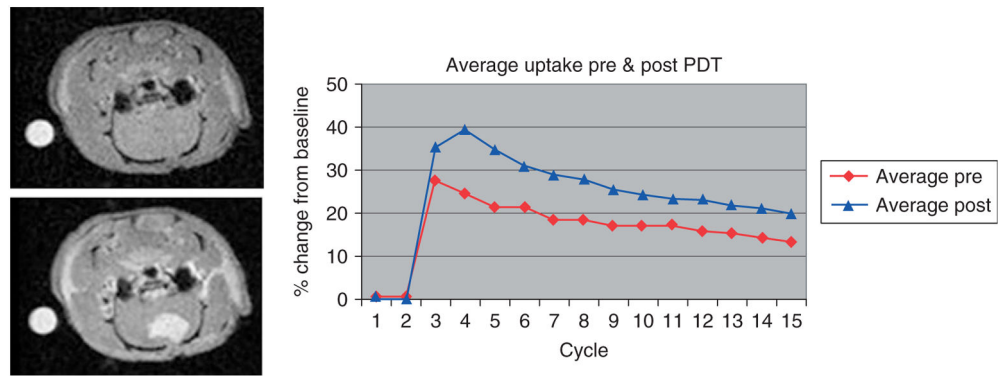
FIGURE 5.
Estimation of affect of photodynamic therapy (PDT) on U87 glioma implant in a rat model using dynamic contrast-enhanced magnetic resonance imaging (DCE-MRI). DCE-MRI images of a U87 glioma implant in a rat model acquired before (left upper) and immediately after (left lower) intravenous injection of Gd-DTPA contrast agent. Analysis of the dynamic uptake (right) revealed that contrast uptake was increased as evidenced by higher peak signal level in MRI images acquired following PDT. The images were acquired using a fast low angle shot (FLASH) sequence (*TR/TE* = 200/3 ms).
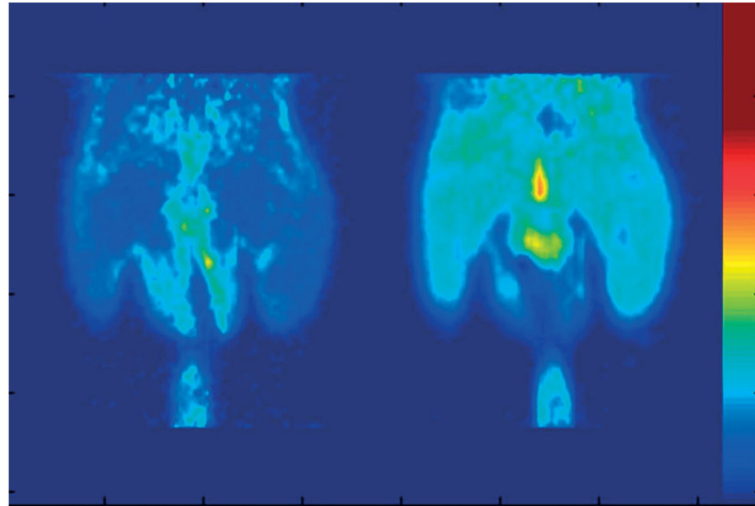
FIGURE 6.
Positron emission tomography (PET) images of a rat injected with 6-deoxy-6-[18F]fluoro-d-glucose ([18F]6FDG) and scanned during glucose clamp under fasting (left) and hyperinsulimic (right) conditions. The tissue concentration of [18F]6FDG was elevated in response to insulin stimulation (Images courtesy of Dr. Raymond Muzic, Case Western Reserve University, Cleveland, OH, USA).
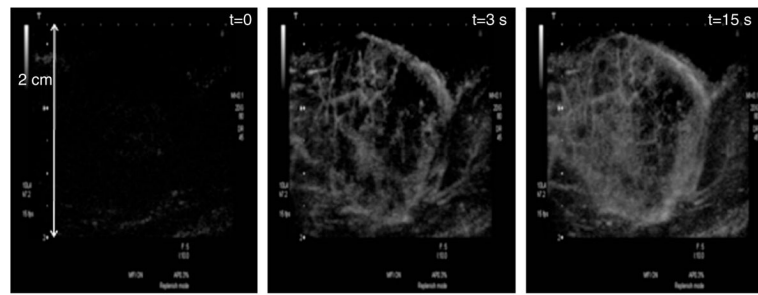
FIGURE 7.
Contrast-enhanced US images of microvasculature of a rat tumor at different delay times after the US contrast agent (UCA) injection. The microvasculature can not be seen in the image acquired at the beginning of the UCA injection (left), whereas, it can be properly delineated in the images acquired after delay times of 3 (center) and 15 s (left) (Images courtesy of Dr. Agata Exner, Case Western Reserve University, Cleveland, OH, USA).
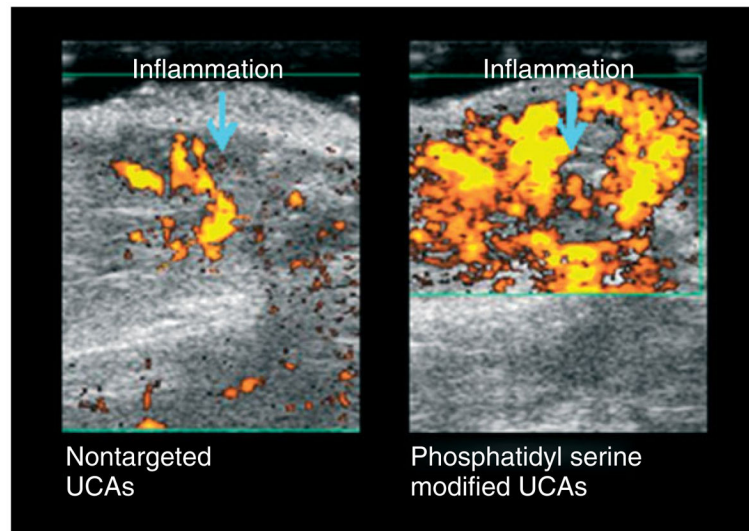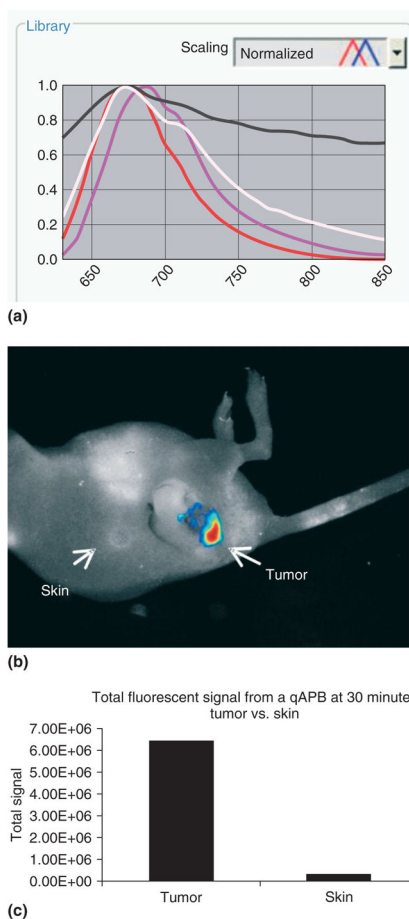
FIGURE 8.
Contrast-enhanced US images of a rat tumor obtained 7 days after performing the ablation therapy. Inflammatory region can readily be identified because of US contrast agent (UCA) targeting by phosphatidyl serine. The images were taken 12 min after injection of phosphatidyl serine UCAs. (Images courtesy of Dr. Agata Exner, Case Western Reserve University, Cleveland, OH, USA).

FIGURE 9.

Spectral analysis can be performed to quantify tumor-specific probe activation using a Maestro™ small animal *in vivo* imaging system. Here, a quenched activity-based imaging probe was injected intravenously and labeled a tumor *in vivo*. Total fluorescent signal from the tumor and the normal skin is quantified. (a) Spectral curves for each fluorophore as well as for autofluorescence can be generated and saved into a spectral library. Individual curves: white, mouse body; black, imaging stage; red, probe *in vivo*; magenta, pure probe. (b) By using spectral decomposition and artificial coloration for each spectral curve, a composite image is obtained. A 'hotmap' of the probe *in vivo* shows total fluorescent intensity of the imaging probe within the tumor. (c) Regions of interest can be delineated manually for quantitative analysis of images. (Image courtesy of Jennifer Cutter, NFCR Center for Molecular Imaging, Case Western Reserve University, Cleveland, OH, USA).
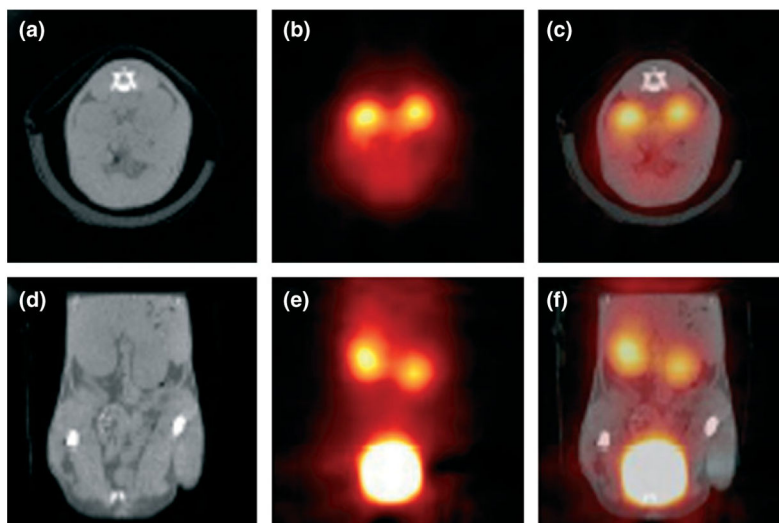
FIGURE 10.
Simultaneous *in vivo* 18F-FDG-positron emission tomography (PET) and computed tomography (CT) scans of a mouse 50 min after injection of 8.5 MBq of [^{18}F]FDG. Note the strong signal in the kidneys and bladder in the PET images (transverse slice in (b), coronal slice in (e)) and the corresponding position of the kidneys and bladder in the CT images (transverse slice in (a), coronal slice in (d)). The fused transverse slice is shown in (c) and the coronal slice in (f). The scan was acquired using 200 views within a total scan time of 18 min. (Reprinted with permission from Ref 259. Copyright 2002 IOP Publishing Ltd.).